Geochemistry and geochronology of the Sierra de Gomez Limestone-hosted U deposit, Chihuahua: Implications for distribution of Rio Grande rift mineral deposits in northern Mexico

Janet Villarreal-Fuentes [a], Gilles Levresse [a,*], Angel F. Nieto-Samaniego [a], Paul Alexandre [b], Rodolfo Corona-Esquivel [c]

[a] Centro de Geociencias, Universidad Nacional Autónoma de México, Blvd. Juriquilla No. 3001, Querétaro 76230, Mexico
[b] Queens University Ontario, Canada
[c] Instituto de Geología, UNAM, Ciudad Universitaria, Mexico

ABSTRACT

Uranium deposits form in a variety of settings. They are partially controlled by the secular evolution of Earth processes, including deposits in extension-related settings such as the intra-cratonic Rio Grande rift. Plio-Quaternary volcanism, mineral deposits, and hydrothermal spots occur along the Chihuahua Central Graben. The age of the Sierra de Gomez U-deposit is 1.8 Ma (based on LA-MC-ICP-MS dating on a uranophane monocrystal), which is contemporaneous with the late mineralization event of the Peña Blanca U-deposit, as well as Rio Grande Rift (RGR)-type deposits in Chihuahua and intraplate volcanism. Studies of fluid inclusions in fluorite and late calcite indicate the presence of hydrocarbons and CH_4-rich brine. Homogenization temperatures range from 87 to 112 °C, and the mean composition (2.0 mol NaCl and 0.3 mol CaCl with CH_4) is comparable to mineralizing brines in MVT deposits and carbonated hydrocarbon reservoirs. Evolution of C and O stable isotopic values for the calcite cement in the Sierra de Gomez Limestone-hosted U deposit illustrates that two separate calcite precipitation events occurred: (1) travertine filling karst structures in the presence of meteoric water and (2) U mineralization during deep hydrothermal fluid circulation that included interactions with a heat source and basement leaching. In a regional context, a metallogenic model suggests that the Chihuahua Trough area is deep enough to generate fluid migration by hydrothermal and/or compaction processes through RGR extensional faults until a favorable trapping horizon is reached. This causes uranium precipitation because water/rock interaction processes generate a local redox barrier.

© 2016 Elsevier B.V. All rights reserved.

1. Introduction

Mineral deposits are heterogeneously distributed in both space and time. They are formed by a variety of natural processes that concentrate elements at an economic grade. The elemental type, character, and abundance reflect the geodynamic environment in which they formed (Cawood and Hawkesworth, 2013). Mineral deposits are considered to be indicators of the evolution of magmatic, hydrothermal, and tectonic processes over geological time. In addition to the direct generation of magmas, asthenospheric upwelling is a powerful heat source in the crust. These phenomena induce crustal scale hydrothermal circulation, which may result in a wide range of ore deposits in intra-cratonic rift systems; one example is the Rio Grande rift (RGR; McLemore and North, 1984; McLemore et al., 1998; Lueth et al., 2005 and references therein). Uranium (U) deposits form in a variety of settings and are

partially controlled by the secular evolution of Earth processes (Cuney, 2010). These include deposits in extension-related settings such as the intra-cratonic Rio Grande rift (McLemore and North, 1984; McLemore et al., 2002; McLemore, 2011).

The RGR is a major tectonomagmatic feature of the North American craton (Fig. 1). Physiographically, this rift is recognized as a series of graben and half-graben structures that can be traced at the surface for over 1000 km, from south-central Colorado until their disappearance in northern Chihuahua, Mexico (Fig. 1; Seager, 1981; Seager et al., 1987; Baldridge et al., 1984; Baldridge, 2004; Keller et al., 1991; Keller and Cather, 1994; DeAngelo and Keller, 1988; Seager, 1995; Seager, 1995, Seager et al., 1987; Torres et al., 1999; Jimenez and Keller et al., 1991; McLemore et al., 2002; Goteti and Mitra, 2013; Cosca et al., 2014; Morton and Bilek, 2014; Koptev et al., 2015; among others). In southern New Mexico and northern Chihuahua, the Rio Grande rift and the Basin and Range province overlap and are not physiographically distinguishable. They share a common style of deformation and are relatively continuous through time. Geophysical, structural, petrographical, geochemical, and geochronological studies in New Mexico, west Texas

* Corresponding author.
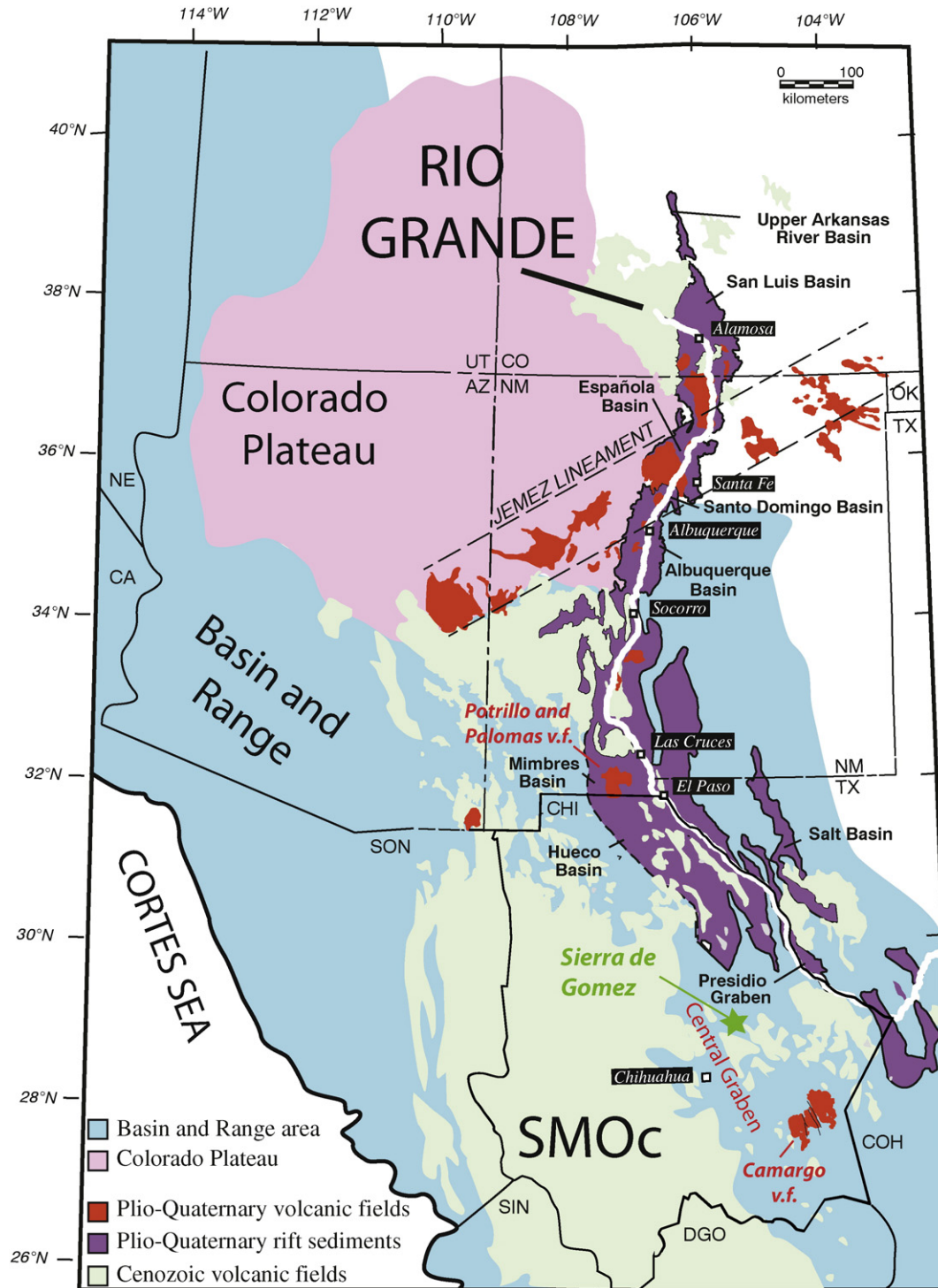   E-mail address: glevresse@gmail.com (G. Levresse).

Fig. 1. Main features of the Rio Grande rift, showing basins and the precursory and associated volcanic fields, modified from Hudson and Grauch (2013). The Cenozoic volcanism shape is modified from Ferrari et al. (2005) and the Basin and Range shape and Colorado Plateau are modified from Baldridge (2004). SON: Sonora, CHI: Chihuahua, TX: Texas, OK: Oklahoma, UT: Utah, CO: Colorado, AZ: Arizona, CA: California, NM: New Mexico, COH: Coahuila, DGO: Durango, SIN: Sinaloa.

and adjacent Mexico have elucidated the history of the RGR from 27 Ma to the present (Reiter and Tovar, 1982, Seager et al., 1987; Baldrige et al., 1984; Keller et al., 1991; DeAngelo and Keller, 1988; Seager, 1995; Seager, 1995, Seager et al., 1987; Lawton and McMillan, 1999; Ragnarsdottir and Charlet, 2000; Haenggi, 2002; among others). The region underwent two main phases of extension: low-angle faulting and shallow basin creation (30–18 Ma), followed by high-angle faulting and graben creation (10–5 Ma; Keller et al., 1991; Wilson et al., 2005). Volcanism began at approximately 13 Ma, occurring along and adjacent

to the Rio Grande rift valley (Chapin et al., 2004). Alkali olivine basalts first appeared along the southern border of New Mexico at approximately 13 Ma, when the crust became critically extended (Chapin et al., 2004). The youngest volcanism occurs along the Jemez Lineament (at approximately 40 ka) in northeastern New Mexico (Chapin et al., 2004). The RGR is associated with high heat flow, vertical movements, seismic activity and fault scarps (King and Metcalfe, 2013). Geothermal anomalies within the rift system are associated with strike-slip faults, accommodation zones, and fault intersections (Easley et al., 2011).

The lithospheric deformed zone is approximately four times the width of the surface expression of the rift. Relatively low amounts of vertical mantle upwelling and small-scale convection limited the amount of heat delivered to the shallow rift, resulting in a small volume of volcanism compared to other rift systems (Wilson et al. 2005). The RGR's southern continuation is well defined along the Rio Grande and the Chihuahua/New Mexico and western Texas borders, and some authors suggest that the Rift could extend as far as the Los Muertos basin in north-central Chihuahua (Baldridge et al., 1984; Lueth et al., 2005; Averil and Miller, 2013). There are few geophysical, geological, and geochronological investigations of the RGR in central Chihuahua. Plio-Quaternary volcanism is almost absent in the area, with the exception of intraplate volcanism of the Camargo field at the southern Chihuahua state border, and the main structures of the RGR are not distinguishable from those of the Basin and Range province.

In this study, we present new geological, geochronological, and geochemical data (including fluid inclusions and stable isotopes) for the limestone-hosted U mineralization deposit in the Sierra de Gomez, Chihuahua. Based on these new data and a regional compilation of extensional geological evidence from the Plio-Quaternary to the present, we discuss a detailed metallogenic model for the Sierra de Gomez uranium deposits in the context of regional geodynamics.

2. Regional geologic setting

The Sierra de Gómez range is located in the western part of the physiographic region of the Chihuahua tectonic belt (Hennings, 1994; Haenggi, 2002; Fig. 1). The region is characterized by a succession of ranges and endorheic basins. The crystalline basement is Greenvillian to early Jurassic in age (Mauger and McDowell, 1983; Tritlla et al., 2004; Villarreal et al., 2014). During the Paleozoic, the Chihuahua region formed the southern passive margin of the continent Laurentia. Between the Triassic and the lower Jurassic, the Pedregosa back arc basin was a dominant paleo-structure (Stern and Dickinson, 2010; Averil and Miller, 2013). During the Mesozoic, this structure developed into to the proto-Chihuahua Basin, bounded to the west by the Aldama platform and to the east by the Diablo Platform. This major paleostructure controlled structural and sedimentary evolution in central Chihuahua until the present (Stern and Dickinson, 2010; Villarreal et al., 2014). The Mesozoic limestone succession lies atop an early Jurassic evaporite tread (Hennings, 1994; Haenggi, 2001). The stratigraphic succession was progressively deformed by various events of the Cordilleran orogeny (Sonoma, Nevadian, and Laramide; Villarreal et al. 2014). Finally, the mountains, which are composed of early Triassic to Late Cretaceous sedimentary rocks folded during the Laramide orogeny, are covered by undeformed Cenozoic volcanic sequences (Hennings, 1994; Haenggi, 2001; Villarreal et al., 2014). Cenozoic volcanic flows and detrital materials filled these basins from the Pliocene to the present (Bartolino, 1992; Haenggi, 2001). Cenozoic volcanism in the area has been dated to between 46 Ma and 27.5 Ma (Cameron et al., 1989, and references therein; McDowell et al., 1997; Ferrari et al., 2005). The volcanic deposits have been interpreted to be a member of the Sierra Madre Occidental (SMOc) volcanic province (Fig. 1; Megaw et al., 1988; McDowell et al., 1997; Ferrari et al., 2005; Oviedo-Patron et al., 2010). The first Eocene volcanic flows rest unconformably on Mesozoic rocks and have a low dip angle (Ferrari et al., 2005; Oviedo-Patron et al., 2010). The emplacement of these flows was coeval with extensional events that occurred during the Eocene–Oligocene (Ferrari et al., 2005; Fig. 1). The Oligocene volcanic rocks of the SMOc (approximately 36 Ma; Ar–Ar; Nandigam et al., 2009) are crosscut and covered by undated carbonatitic dykes and flows (Nandigam et al., 2009). Finally, the Camargo volcanic field, which is Plio-Pleistocene in age (4.7–0.09 Ma; Aranda-Gomez et al., 2003), lies midway between the Sierra Madre Occidental and the Trans-Pecos of Texas (Fig. 1). This has been characterized as an intraplate mafic alkalic volcanic event that was strongly controlled by northwest-striking normal faults (Aranda-Gomez et al., 2003).

3. History and geologic setting of the Sierra de Gomez Limestone-hosted U deposit

Interest in uranium as a commodity began in the early 1900s with the discovery of uraninite in the Placer de Guadalupe district a few kilometers east of the Sierra de Gomez. Regional and local exploration, characterization, and pre-industrial production were initiated in the late fifties. The Sierra de Gomez (SG) is a mountain range located 70 km northeast of the city of Chihuahua. The total amount of uranium recovered in the Sierra de Gomez district during six years of production is estimated at 23,000 metric tons of U_3O_8 (with a concentration of 0.27% per metric ton), mostly from the southeastern part of the district. Proven reserves are estimated at 2.500 metric tons of U_3O_8 (with a concentration of 0.36% per metric ton) for the southeastern block and 150,000 metric tons of U_3O_8 (with a concentration of 0.36% per metric ton) for the entire district. Mining ceased in the Sierra de Gomez district in 1968. Exploration activity in Mexico was resumed in 2005 by the Mexican Geological Service.

The outcropping sedimentary strata in the area are Albian to Cenomanian in age. South of the Sierra de Gomez range, the Mesozoic folded sequence is unconformably covered by Cenozoic volcanism (Las Tetas de Juana and the El Infierno range; Fig. 2), which is dated to approximately 45 to 34 Ma (Oviedo-Patron et al., 2010). The Sierra de Gomez range is interpreted as a pair of west-verging fault propagation folds, each with approximately 1.6 km of structural relief (Fig. 2; Haenggi, 2002). These folds converge in the north into a single anticlinal structure that forms the main body of the Sierra de Gomez. Many west-verging contractional structures outcrop along the road that cuts through the Sierra de Gomez (Fig. 2). Both the eastern and western borders of the Sierra de Gomez range are limited by an N–S normal fault that is recognized to be a Basin and Range structure (Lara-Zavala, 1960; Mitchell et al., 1981). The entire range is crosscut by E–W sub-vertical fractures (Fig. 2; Lara-Zavala, 1960; Mitchell et al., 1981). Mineral paragenesis is characterized by several generations of calcite, fluorite, scarce pyrite, Fe-oxides and, at the end of the sequence, hexavalent uranium minerals (including carnotite, $K_2(UO_2)_2(VO_4)_2 1–3H_2O$; metatyuyamunite, $Ca(UO_2)_2(VO_4)_2 3–5H_2O$; tyuyamunite, $Ca(UO_2)_2(VO_4)_2 5H_2O$; and abundant uranophane, $Ca(UO_2)_2(HSiO_4)_2 5H_2O$). Chemistry from U-barren to U-mineralized limestones of the Sierra de Gomez formation shows positive correlation between uranium and nickel, zinc, molybdenum and vanadium. The metal content can reach values of 3% Mo, 2% V, 1.7% Ni, and 2.7% U (Mitchell et al., 1981). Uranium mineralization is also associated with Mg, Ca, and Sr depletion (Mitchell et al., 1981). No regional or local chemical zoning has been reported.

4. Analytical methods

4.1. Petrography

Thin sections were examined under a petrographic Olympus® BX-50 optical microscope using a Qimage Micropublisher 5 Mp digital camera with a Peltier cooled CCD at the Crustal Fluids Laboratory of the Centro de Geociencias (CFL-CGEO) at the Universidad Nacional Autonoma de Mexico (UNAM), Querétaro campus.

Carbonate cements were studied using a Reliotron® cold cathode cathodoluminescence (CL) device attached to an Olympus SZ-X binocular microscope and a Qimage Micropublisher 5 Mp digital camera with a Peltier cooled CCD. The acceleration voltage of the electron beam was 15 kV with a probe current of 500 μA. CL emission was enhanced by observing the quartz samples on a copper plate previously cooled by immersion in liquid nitrogen.

Thin sections were observed using an Olympus BX-50 epifluorescence microscope equipped with a UV light source (Mercury lamp, excitation BP
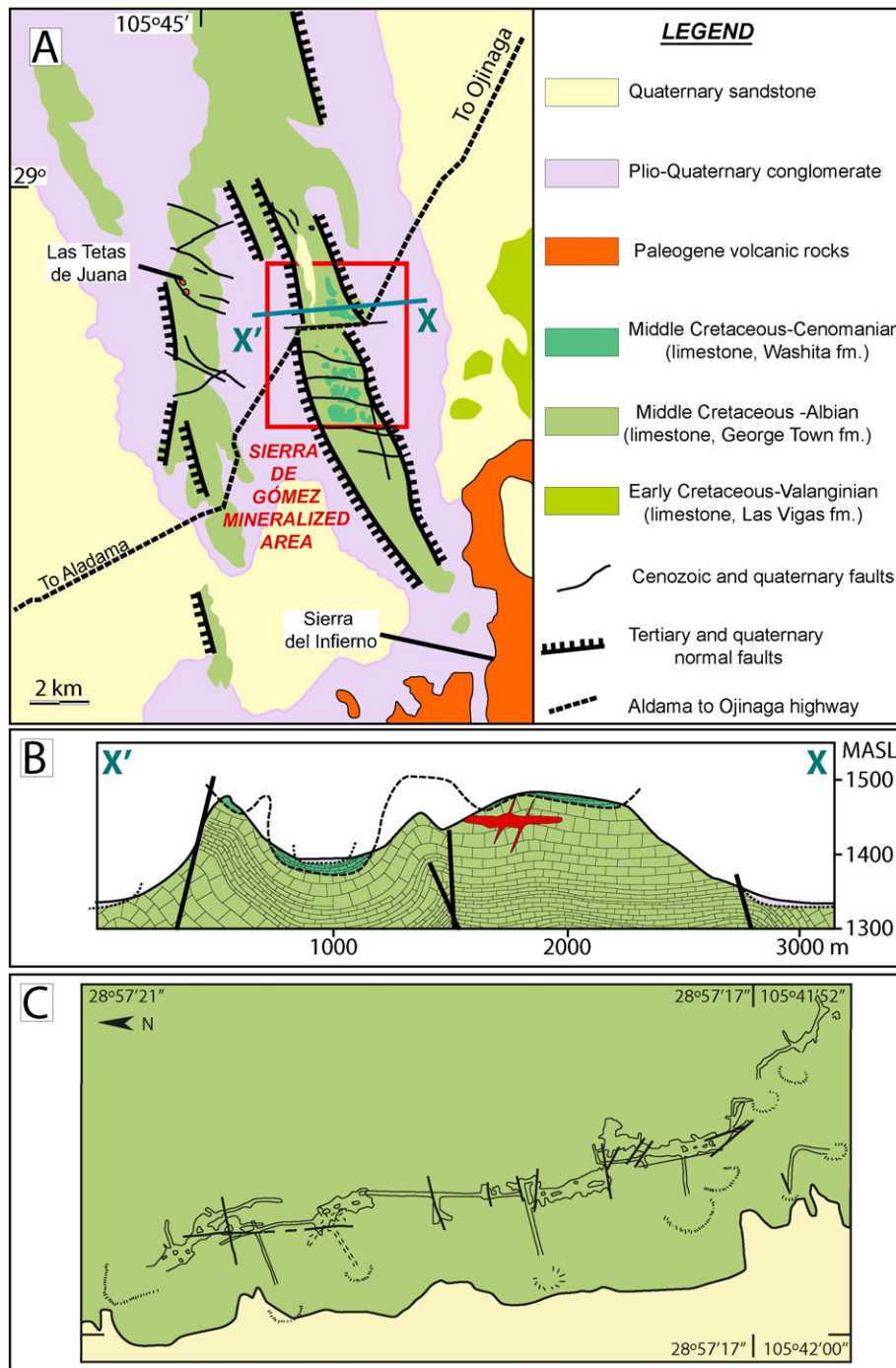
Fig. 2. (A) Simplified geologic map of the Sierra de Gomez range. (B) Simplified geologic cross-section of the Sierra de Gomez U-deposit (modified from Mitchell et al., 1981). (C) Underground mining works of the Sierra de Gomez Limestone-hosted U deposit (modified from Lara-Zavala, 1960); see Fig. 1 for map location.

365/12, dichroic mirror FT 395 and emission LP 397) with a U-MNU2 excitation filter (straight band, 360–370 nm) and a LP400 long-pass emission filter (>400 nm), allowing for recognition of fluorescent hydrocarbon-bearing fluid inclusions.

4.2. C and O stable isotopes

Carbonates were analyzed for their carbon and oxygen stable isotopic composition following the CO_2 extraction method of McCrea (1950). Up to 15 mg of sample was reacted with H_3PO_4 at 50 °C, and the collected CO_2 was analyzed on a Finnigan MAT Delta S thermal ionization mass

spectrometer at the Serveis Científic-Tècnics of the Universitat de Barcelona. The reproducibility of the analyses was better than ±0.1‰ for both isotopes.

4.3. Fluid inclusion microthermometry

Double-polished wafers were obtained from U-mineralized and barren samples. Wafers were inspected under a petrographic Olympus® BX-50 optical microscope with a Qimaging Micropublisher 5 Mp digital camera equipped with a Peltier-cooled CCD. Microthermometric data were acquired on a Linkam THMSG-600 stage attached to an Olympus®

BX-50 petrographic microscope equipped with ultra-long working distance objectives at the Crustal Fluids Laboratory of the Centro de Geociencias at UNAM in Querétaro. This stage permits the observation of fluid inclusion phase transitions from −193 to +600 °C with an accuracy of ±0.1 °C. The stage was calibrated using Synflinc® synthetic fluid inclusions and ultrapure chemicals with a fixed melting point.

4.4. Raman microspectroscopy

Raman microspectroscopy was used to quantify the methane content of the aqueous inclusions. Calibration was based on the area ratio of the stretching band of methane (2917 cm^{-1}) to the stretching band of water (3000 to 4000 cm^{-1}) from spectra acquired on synthetic inclusions (Ortega-Ramirez et al., 2001; Suter, 2001; Aranda-Gomez et al., 2003). The intensity ratio of the Raman bands is highly correlated with methane concentration and the slopes of the regression curves vary slightly with the concentration of sodium chloride. A software algorithm based on the model of Bartolino (1992) was used to calculate the composition of the inclusions at the homogenization temperature. The Raman spectrometer is a High Resolution Labram type (Dilor), equipped with a Notch filter and a grating (1800 grooves per mm) that makes it luminous. The detector is a CCD cooled at −30 °C. The exciting radiation is provided by an Ar^+ laser (Type 2020, Spectraphysics) at 514.5 nm. The spectral resolution is approximately 2 cm^{-1}. The accumulation time, laser power and confocal aperture were modified for each inclusion measurement to obtain an optimum signal to noise ratio.

4.5. Cathodolumiscence and UV microscopy

Recrystalized limestone and calcite cements were studied using a Reliotron® cold cathode cathodoluminescence (CL) device attached to an Olympus SZ-X binocular microscope and a Qimage Micropublisher 5 Mp digital camera with a Peltier cooled CCD. The acceleration voltage of the electron beam was 15 kV, with a probe current of 500 μA. CL emission was enhanced by observing quartz samples on a copper plate previously cooled by immersion in liquid nitrogen.

Thin sections were examined using an Olympus BX-50 epifluorescence microscope equipped with a UV light source (Mercury lamp, λ = 365 nm) with a U-MNU2 excitation filter (straight band, 360–370 nm) and an LP400 long-pass emission filter (>400 nm), allowing for recognition of fluorescent hydrocarbon-bearing fluid inclusions.

4.6. Uranium mineralization geochronology

In-situ U/Pb dating of uraninite was performed on polished thin sections by laser ablation-inductively coupled plasma-multi collector mass spectrometry (LA-MC-ICP-MS) at Queen's University, Canada. The laser used was the Mercantek LUV213 Laser Ablation System with a frequency quintupled Nd-YAG (213 nm) in raster mode. The laser conditions included a laser power output of 40 to 45% (<1 mJ/cm^2), pulses of 50 m/s with a repetition rate of 2 Hz, and a spot size of 25 to 35 μm. The MC-ICP-MS instruments used were made by ThermoFinnigan Neptune and were each equipped with 9 Faraday cups and 1011 Ω amplifiers.

5. Analytical results

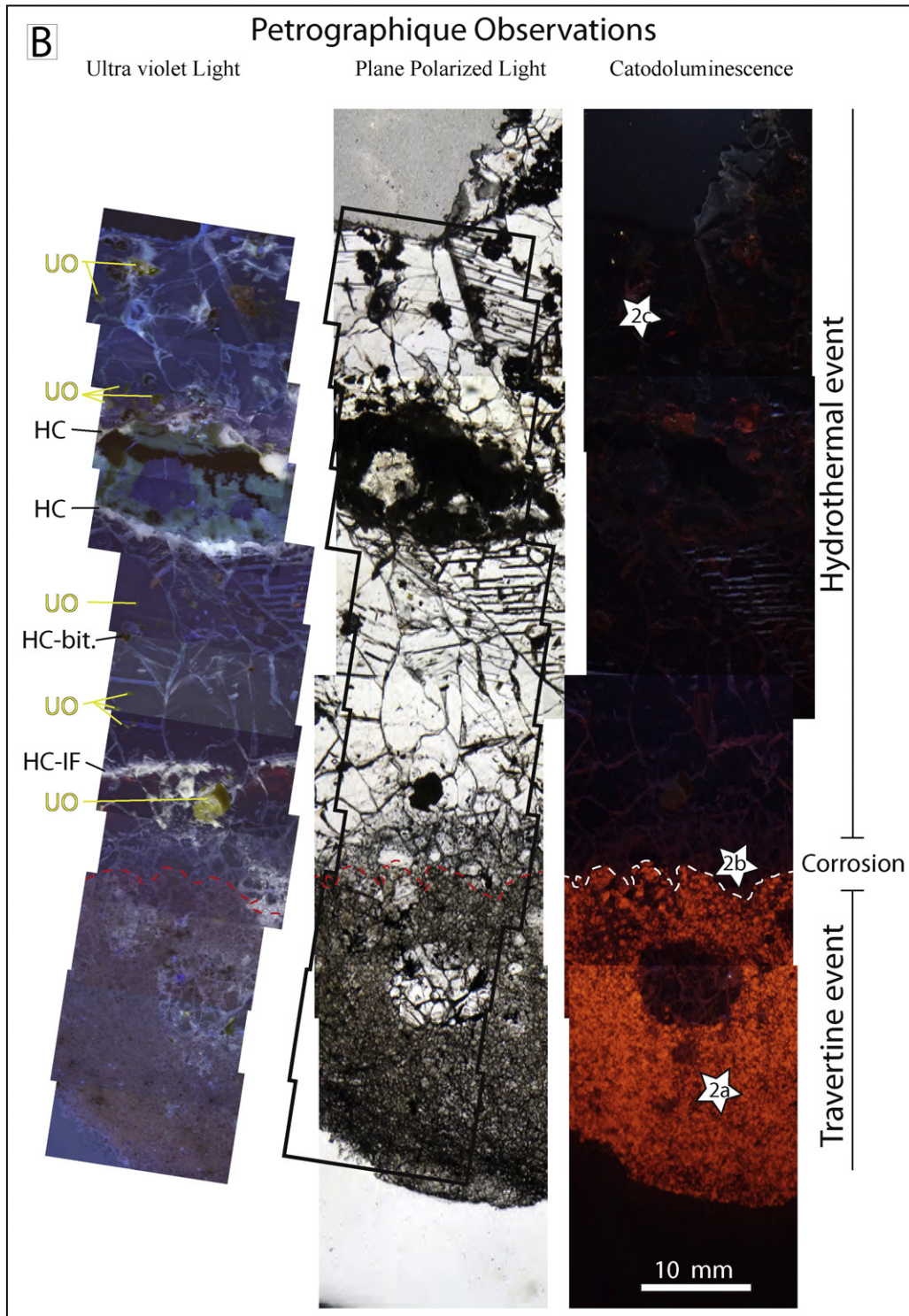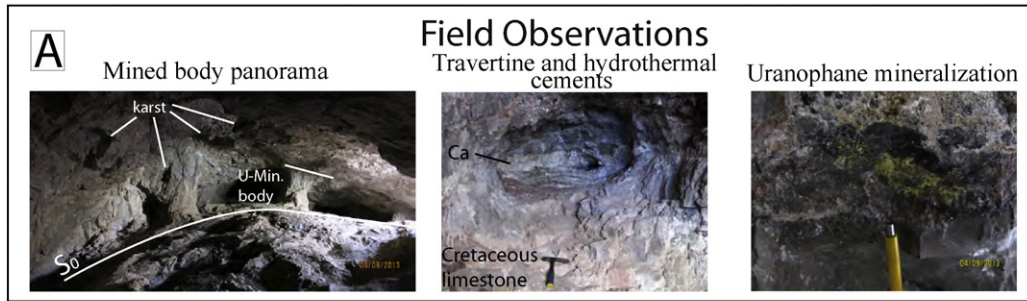### 5.1. Description of the Sierra de Gomez Limestone-hosted U deposit

The host rock is a massive micritic limestone rich in rudists and colonial corals. The earliest phase of cave development produced phreatic passages that follow the limestone bedding and are dissected by faults related to Laramide uplift and extensional deformation (Fig. 3A). The cave passages are older than the extensional Neogene faulting and may be Paleocene in age, preceding the Eocene volcanism observed in the Las Tetas de Juana and El Infierno ranges (Fig. 2; Oviedo-Patron

et al., 2010). These passages were subsequently abandoned once the groundwater conduits were covered by Eocene volcanic flows. Neogene uplift of the sedimentary sequence led to a phase of rejuvenation (Keller and Baldridge, 1999; Ewing, 2013), in which the Eocene volcanic flows were locally eroded and groundwater was introduced through the E–W fault set. During the Quaternary, this erosion intersected the cave passages. The caves are currently dry. Locally, the host rock limestone shows evidence of recrystallization, with increased grain size and porosity. Travertine, as cave and fracture fillings or stalactites, occurs as banded, coarsely crystalline calcite. We use the word "travertine" as a general term for fresh-water carbonate deposits of all types (White, 2008). The transition from limestone and travertine to hydrothermal cements is highlighted by major, pervasive corrosion and is associated with a secondary porosity generation event (Fig. 3B).

The mineralogy of the limestone hosted U deposits in the Sierra de Gomez is simple. The U deposits consist of irregular mineralized bodies that are meters to decameters in size. They preferentially develop along strata, joints, fractures, veinlets and breccia filling pores in the cave. They are usually interconnected by enlarged stratification planes or joints (Figs. 2C and 3). Common paragenetic evolution recorded is demonstrated by several cases shown in Figs. 3 and 4. Crosscutting relationships are extremely complicated and variable at all scales. This inhomogeneity probably reflects the original inhomogeneities of the enclosing rock prior to exposure to U-mineralizing fluids and/or possible fluctuations of the fluid chemistry. The corrosion porosity predates the mineral precipitates (green calcite, chalcedony, fluorite, iron oxides, and uranium oxides; Fig. 3B). These precipitates are also found as cavity infillings within tension gashes, reopened stylolites, and surface coatings, which suggests that the parental fluids were preferentially introduced along discontinuity surfaces. The mineral successions repeat systematically, suggesting that they originated from pulses of hydrothermal fluids. Chalcedony can be locally abundant and is associated with iron oxides and the dissolution of primary limestone textures. In general, early precipitation of silica and iron oxides is followed by late calcite. Both silica and calcite show uranium oxide inclusions. Locally, purple fluorite grows over the silica generations, and can form the base for a second green calcite and uranium oxide generation (Figs. 3 and 4). Hydrocarbons (methane and bitumen) occur within the silica and green calcite when they are in direct contact with the limestone. Uranium oxides are also found in the recrystallized limestone aureoles, and as coating on diaclasts. Carnotite ($K_2(UO_2)_2(VO_4)_2 1–3H_2O$), metatyuyamunite ($Ca(UO_2)_2(VO_4)_2 3–5H_2O$), and, mainly, uranophane ($Ca(UO_2)_2(HSiO_4)_2 5H_2O$) were confirmed by XRD analysis. A late event is represented by the precipitation of malachite ($Cu_2CO_3(OH)_2$), smithsonite ($ZnCO_3$), cerussite ($PbCO_3$), aurichalcite (($(Zn,Cu)_5(CO3)_2(OH)_8$), and zaratite ($Ni_3CO_3(OH)_4 4H_2O$). Finally, a set of unmineralized white calcite crosscuts the entire paragenetic sequence.

5.2. Study of fluid inclusions

Six wafers were selected for microthermometric analysis (n = 44 in green calcite). The recrystallized limestone and the travertine are devoid of measurable fluid inclusions. Only the green mineralized calcite contains aqueous and hydrocarbon-rich primary fluid inclusions suitable for microthermometric analyses. In all of the selected samples, the fluid inclusion assemblages include primary fluid inclusions, either isolated or along growth zones, as well as pseudosecondary fluid inclusions trapped along fracture planes. Oil-bearing fluid inclusions were also found within the fluorite by UV microscopy; however, due to their minute size, they were not appropriate for microthermometric analysis. Within the green calcite, aqueous and hydrocarbon-rich inclusions never occur in the same plane. Three fluid inclusions types were found: (1) rare monophase, vapor-rich fluid (V) inclusions without any observable liquid phase; (2) undersaturated, brine-bearing biphasic fluid inclusions (Fig. 5); and (3) hydrocarbon-bearing biphasic fluid

Field Observations

Mined body panorama

Travertine and hydrothermal cements

Uranophane mineralization

Petrographique Observations

Ultra violet Light

Plane Polarized Light

Catodoluminescence

inclusions. Aqueous and hydrocarbon-rich inclusions never occur in the same plane.

The hydrocarbon vapor-rich inclusions (Type 1) are primary. They are elongated, up to 60 mm long, and are mainly distributed along the growth rim of the green calcite (see Fig. 5). These fluid inclusions could not be measured by microthermometry because no liquid-rich rim was apparent after the freezing runs; this is probably due to optical limitations and the calcite refraction index. However, their composition was characterized using Raman spectroscopy.

The aqueous fluid inclusions (Type 2) were measured in the green calcite. Type 2 is represented by irregularly shaped fluid inclusions with a median diameter of 150 mm. The liquid-to-vapor ratio is close to 0.8.

Under UV light, all of the hydrocarbon-bearing fluid inclusions (Types 1 and 3) trapped in fluorite and green calcite show a homogeneous fluorescence color that ranges from pale to bright yellow, suggesting the presence of one light oil type.

Fluid inclusion microthermometry and Raman spectrometry results are presented in Fig. 5 and Table 1. Type 1: Raman measurements of Type 1 indicate that the hydrocarbon fluid composition is mainly ethane, and there is a significant methane concentration in the Type 2 aqueous fluid inclusions. Type 2: The homogenization temperatures (Th) of the bubble shrinkage fluid inclusions range from 87 to 112 °C. A high-relief phase identified as hydrohalite melted between −22.1 and −21.8 °C. The Tmi values range from 10.2 to −9.1 °C. The total salinity was calculated using an equation from Oakes et al. (1990) and ranges from 12.5 to 14.9 wt%. In Fig. 5A and B, the aqueous-bearing fluid inclusions have a small range of homogenization temperatures and salinity, indicating that mixing did not occur and suggesting that the precipitation process may have involved adiabatic cooling.

5.3. C and O stable isotopic compositions: origin of the major corrosion

Host rock limestones and calcites were sampled from the Sierra de Gomez mineralizing area and were analyzed in a paragenetic sequence based on petrographic, ultraviolet microscopy and cathodoluminescence observations (Fig. 3 B). The C and O stable isotopic compositions are reported in per mil relative to VPDB (Table 2; Fig. 6). The data are grouped by sample and the paragenetic stage of the U-barren travertine and U-mineralizing hydrothermal events (Fig. 6).

The $\delta^{13}C_{PDB}$ and $\delta^{18}O_{PDB}$ values determined from the host rock limestone have relatively restricted ranges, from 2.6‰ to 3.7‰, and from −8.6‰ to −7.9‰, respectively. Travertine cements present large variations in $\delta^{18}O_{PDB}$ values, from −6.9‰ to −1.9‰, and their $\delta^{13}C_{PDB}$ values ranges from −9.4‰ to −7.7‰. However, the U-mineralized calcite showed a different distribution of stable isotopic values, with $\delta^{13}C_{PDB}$ and $\delta^{18}O_{PDB}$ values ranging, respectively, from −12.0‰ to −9.1‰ and −1.9‰ to 1.9‰ (Fig. 5). Fig. 5 shows that the different patterns of the $\delta^{18}O_{SMOW}$ and $\delta^{13}C_{PDB}$ values of the travertine concretions and the U-mineralized calcite correspond to two different formation processes.

5.4. U mineralization geochronology

U–Pb dating of uranophane in the Sierra de Gomez Limestone-hosted U deposit was performed to determine the chronology of the extensional event(s) related to uranium transport and deposition. The disseminated uranophane grains sampled from the Sierra de Gomez deposit rarely exceed the millimeter scale.

Nineteen analyses were carried out on disseminated uranophane grains from the Sierra de Gomez U-mineralizing area. They showed $^{206}Pb/^{238}U$ ages ranging from 3.0 ± 0.5 Ma to 1.1 ± 0.2 Ma and $^{207}Pb/^{235}U$ ages ranging from 3.1 ± 1.1 Ma to 0.9 ± 0.7 Ma (Table 3). All ages are concordant (Fig. 7A; Table 3), and all of the analyses form a single group if the errors are considered. A statistical distribution allows the identification of three main crystallization events. The most common event consists of a tight cluster of concordant ages (n = 16) with a weighted mean $^{207}Pb/^{206}Pb$ age of 1.8 ± 0.1 Ma (n = 16; MSWD of 0.52; Fig. 4A). The second event (n = 2) has an older weighted mean $^{207}Pb/^{206}Pb$ age of 3.1 ± 1.5 Ma (n = 2; MSWD of 0.005; Fig. 7A). A final event is represented by only one result, with an age of 1.1 ± 0.2 Ma. In summary, U–Pb dating of mono-crystalline uranophane reveals three different mineralization pulses at 3.1 ± 1.5 Ma, 1.8 ± 0.1 Ma, and 1.1 ± 0.2 Ma.

The Sierra de Gomez uranophane ages coincide with Pliocene to Quaternary metallogenic and volcanic activities in Chihuahua, southern New Mexico, and Texas (Fig. 7B). Uranophane U–Pb dating of the Sierra de Gomez U-deposit clearly illustrates the episodic character of the hydrothermal system, indicating three distinct pulses over approximately 2 million years. The Sierra de Gomez U-deposits were synchronous within error with late primary and altered Peña Blanca U-deposits and are contemporary with the formation and alteration of the final RGR-type deposit (5.4 to 2.3 Ma; Lueth et al., 2005; Fig. 7B), as well as the main intraplate volcanism event in Chihuahua (3.0 to 1.5 Ma; Aranda-Gomez et al., 2003 Fig. 7B). The age distribution diagram suggests that a regional extension and fluid circulation event occurred in the southern part of the central Chihuahua area.

6. Discussion

6.1. Metallogenic model of the Sierra de Gomez Limestone-hosted U-deposit

Metallogenic models of mineral deposits place three major steps within a chronological context: the metal source, transport, and trap characterization. Limestone-hosted U-deposits are considered to be anomalous in uranium metallogenesis (Cuney, 2009). Limestone is typically an unfavorable host rock for uranium because of its relatively low permeability and porosity and the absence of precipitating agents (McLemore, 2011). However, a set of unusual geological circumstances allowed the formation of uranium deposits in the Sierra de Gomez Limestone and some areas in New Mexico (McLemore, 2011).

Petrography and the C and O stable isotopic evolution of the travertine and U-mineralized calcite suggest the existence of two calcite cementation events. The vertical isotopic evolution of the travertine concretions suggests a shallow stratigraphic position that allowed interaction with the karstic host rock and a freshwater meteoric phreatic system (Goldstein et al., 2010). The trend of marked depletion in $\delta^{13}C_{PDB}$ values at the base of the travertine fillings (Fig. 5) and the enrichment in $\delta^{13}C_{PDB}$ values over time (Fig. 5) suggests that an initial input of bicarbonate with low $\delta^{13}C_{PDB}$ values from soil organic processes occurred, followed by the progressive addition of bicarbonate with high $\delta^{13}C_{PDB}$ values from interaction with the limestone host rock. The U-mineralized calcite isotopic values form a line connecting the isotopic values of the local limestone host rocks and the isotopic values of standard hydrothermal calcite; this could represent a mixing line. This chemical evolution suggests water/rock interactions between the U-mineralizing hydrothermal fluids and the limestone host rocks. Low $\delta^{18}O_{PDB}$ values throughout the paragenetic evolution (see the evolution of samples 3 and 4) indicate that the water/rock processes were

Fig. 3. (A) 1 — Underground panorama photography; 2 — Travertine and hydrothermal cement filling karst spaces (ca: Calcite; F: Fluorite), and 3 — Uranium mineralization coated in travertine cement. (B) Microphotographic images under plane polarized light, cathodoluminescence and ultraviolet light of the travertine and hydrothermal calcite cements and uranium mineralization from sample SG-2. Corrosion event 2 at the contact of the travertine and hydrothermal cements (dashed line) is followed by a hydrocarbon halo. White stars indicate microsampling for stable isotopic analysis.
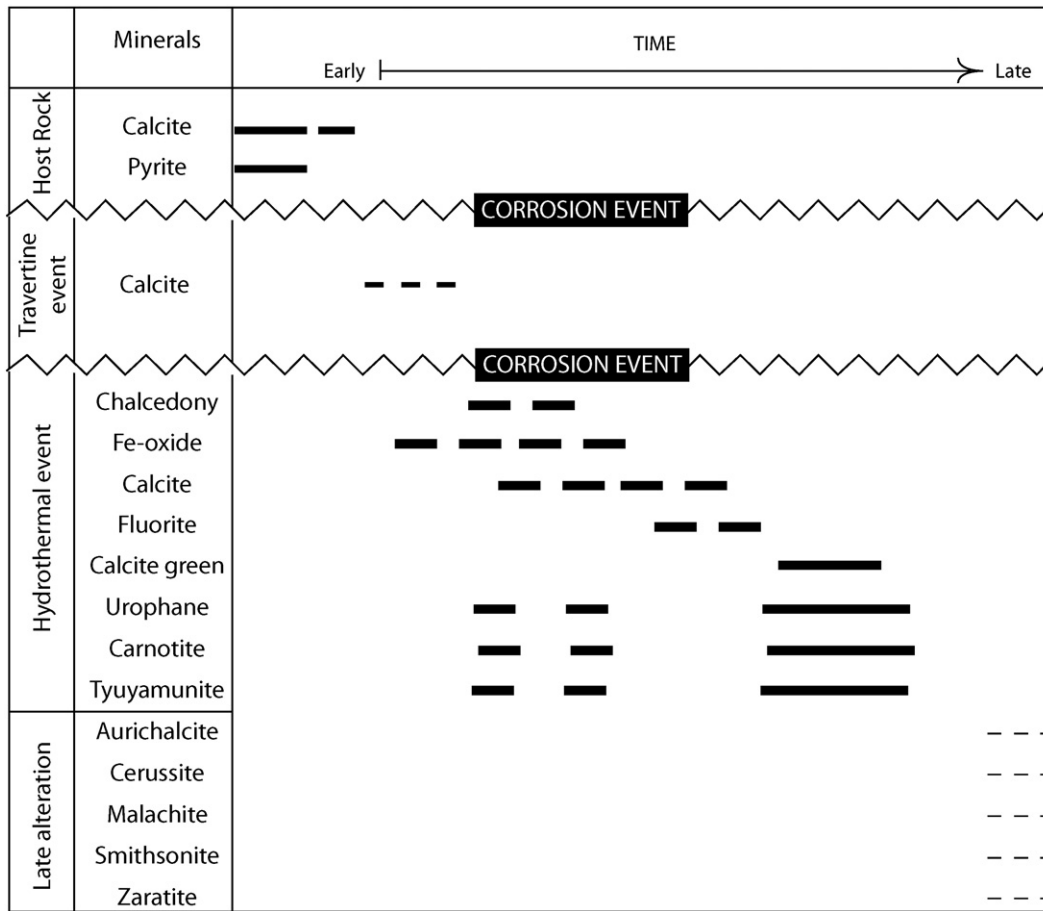
Fig. 4. Paragenetic sequence of the Sierra de Gomez Limestone-hosted U deposit.

dominated by mineralizing hydrothermal fluids. These values also suggest that organic matter was introduced into the system, as observed in the fluid inclusion petrography.

Prior to the U-mineralizing events, the shallow parts of the limestone host rock interacted with meteoric water that was probably recharged in upland margins. As a result, the karst spaces were filled
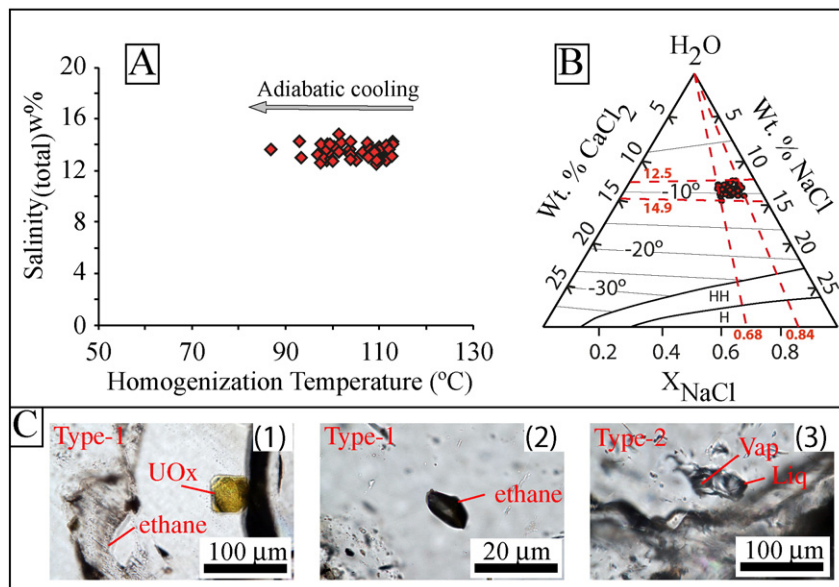
Fig. 5. (A) Temperature vs. salinity plot for the hydrothermal fluid inclusion generations in the U-mineralized calcite. (B) Ternary vapor-saturated liquidus phase diagram for the system H_2O–$NaCl$–$CaCl_2$ (modified from Oakes et al., 1990). H: Halite; HH: Hydrohalite. (C) Fluid inclusion photomicrography: (1) Primary monophasic gas-dominant fluid inclusions along the calcite growth zone, (2) Monophasic gas-dominant fluid inclusions (Type 1), and (3) Hydrothermal biphasic (Type 2; liquid and vapor) hydrothermal fluid inclusions.

Table 1
Microthermometric data and Raman spectrometric characterization of typical fluid inclusions of the Sierra de Gomez diagenetic and hydrothermal calcites.

Sample	Minerals	Event	Th	Tmi hydrohalite	Tf	Salinity total	m(NaCl)	m(CaCl$_2$)	NaCl/(NaCl + CaCl$_2$)
			(°C)	(°C)	(°C)	(wt.%)			
SG-2	Green calcite	Type-2	93.20	−22.1	−9.1	13.0	2.0	0.3	0.80
SG-2	Green calcite	Type-2	86.70	−22.3	−9.7	13.7	2.1	0.3	0.77
SG-2	Green calcite	Type-2	107.30	−22.8	−10.2	14.2	2.0	0.4	0.72
SG-2	Green calcite	Type-2	98.60	−21.7	−8.9	12.8	2.1	0.2	0.84
SG-2	Green calcite	Type-2	103.50	−22.1	−9.7	13.7	2.2	0.3	0.79
SG-2	Green calcite	Type-2	101.70	−23.1	−10.2	14.2	2.0	0.5	0.69
SG-2	Green calcite	Type-2	111.30	−21.9	−8.9	12.8	2.1	0.2	0.80
SG-2	Green calcite	Type-2	110.90	−22.3	−9.5	13.5	2.1	0.3	0.77
SG-2	Green calcite	Type-2	112.70	−22.3	−10.3	14.3	2.2	0.3	0.77
SG-2	Green calcite	Type-2	97.30	−22.5	−8.7	12.6	1.9	0.3	0.70
SG-2	Green calcite	Type-2	106.30	−21.8	−9.5	13.5	2.2	0.2	0.80
SG-6	Green calcite	Type-2	92.80	−22.3	−10.3	14.3	2.2	0.3	0.77
SG-6	Green calcite	Type-2	96.70	−22.9	−9.3	13.3	1.9	0.4	0.71
SG-6	Green calcite	Type-2	98.20	−22.1	−9.1	13.0	2.0	0.3	0.79
SG-6	Green calcite	Type-2	99.50	−22.7	−9.0	13.0	1.9	0.4	0.70
SG-6	Green calcite	Type-2	99.10	−21.8	−9.5	13.5	2.2	0.2	0.83
SG-6	Green calcite	Type-2	98.80	−21.9	−10.1	14.1	2.3	0.3	0.82
SG-6	Green calcite	Type-2	98.60	−22.4	−9.7	13.7	2.1	0.3	0.76
SG-6	Green calcite	Type-2	97.40	−22.8	−10.1	14.1	2.0	0.4	0.72
SG-11	Green calcite	Type-2	100.20	−22.6	−9.9	13.9	2.0	0.4	0.71
SG-11	Green calcite	Type-2	103.70	−22.9	−10.3	14.3	2.0	0.4	0.71
SG-11	Green calcite	Type-2	101.20	−23.2	−10.9	14.9	2.0	0.5	0.68
SG-11	Green calcite	Type-2	109.90	−21.7	−8.9	12.8	2.1	0.2	0.84
SG-11	Green calcite	Type-2	103.70	−22.9	−9.3	13.3	1.9	0.4	0.71
SG-11	Green calcite	Type-2	109.80	−21.9	−9.9	13.9	2.3	0.3	0.82
SG-23	Green calcite	Type-2	99.30	−22.2	−10.1	14.1	2.2	0.3	0.78
SG-23	Green calcite	Type-2	101.20	−23.1	−9.5	13.5	1.8	0.4	0.69
SG-23	Green calcite	Type-2	107.90	−22.7	−9.7	13.7	2.0	0.4	0.73
SG-23	Green calcite	Type-2	104.90	−22.1	−8.9	12.8	2.0	0.3	0.79
SG-23	Green calcite	Type-2	99.90	−22.5	−8.8	12.8	1.9	0.3	0.75
SG-23	Green calcite	Type-2	103.70	−21.7	−9.0	12.9	2.2	0.2	0.84
SG-24	Green calcite	Type-2	110.60	−21.9	−9.6	13.6	2.2	0.3	0.82
SG-24	Green calcite	Type-2	112.70	−22.9	−10.1	14.1	2.0	0.4	0.71
SG-24	Green calcite	Type-2	110.30	−23.1	−9.7	13.7	1.9	0.4	0.69
SG-24	Green calcite	Type-2	109.20	−23.2	−8.6	12.5	1.7	0.4	0.68
SG-24	Green calcite	Type-2	110.00	−22.7	−9.7	13.7	2.0	0.4	0.73
SG-24	Green calcite	Type-2	107.60	−23.2	−9.2	13.2	1.8	0.4	0.68
SG-24	Green calcite	Type-2	111.30	−22.9	−10.0	14.0	2.0	0.4	0.71
SG-27	Green calcite	Type-2	108.80	−22.8	−9.6	13.6	1.9	0.4	0.72
SG-27	Green calcite	Type-2	111.90	−22.3	−9.7	13.7	2.1	0.3	0.77
SG-27	Green calcite	Type-2	112.50	−21.8	−9.2	13.1	2.2	0.2	0.83
SG-27	Green calcite	Type-2	108.80	−22.4	−9.5	13.5	2.0	0.3	0.76
SG-27	Green calcite	Type-2	109.30	−22.0	−8.9	12.8	2.0	0.3	0.81
SG-27	Green calcite	Type-2	107.50	−22.8	−9.1	13.1	1.9	0.4	0.72

with travertine cement (Fig. 3). The transition between the two events is petrographically highlighted by corrosion, suggesting a different fluid composition. The calcite U-mineralizing cement has inclusions of uranium oxide and hydrocarbons (liquid, gas, and bitumen). Surdam and Yin (1994) note that organic acids play an important role in porosity generation in carbonate oil reservoirs. Organic acids are released

Table 2
C and O stable isotopic values for the Sierra de Gomez limestone and travertine and hydrothermal calcite cements.

| Sample	Event	δ^{13}C (PDB)	δ^{18}O (PDB)	δ^{18}O (SMOW)
		(‰)	(‰)	(‰)
Albian limestone	Host rock	−8.6	3.5	22.0
Albian limestone	Host rock	−7.9	3.7	22.8
Albian limestone	Host rock	−8.5	2.6	22.0
SG-1a	Early diagenic conc.-1	−7.7	−6.9	22.9
SG-1b	Early diagenic conc.-1	−7.7	−6.9	22.9
SG-1c	Early diagenic conc.-2	−8.6	−5.6	22.0
SG-1d	Early diagenic conc.-3	−8.7	−4.8	21.8
SG-1e	Early diagenic conc.-4	−8.7	−3.8	21.9
SG-2a	Early diagenic conc.-1	−8.2	−6.9	22.4
SG-2b	Early diagenic conc.-2	−9.4	−1.9	21.2
SG-2c	Late calcite-3	−10.6	0.7	19.9
SG-3a	Late calcite-1	−9.1	1.9	21.4
SG-3b	Late calcite-2	−11.5	1.2	19.0
SG-4a	Late calcite-1	−11.7	0.0	18.8
SG-4b	Late calcite-4	−11.7	−0.4	18.8
SG-4c	Late calcite-3	−11.8	−1.9	18.7
SG-4d	Late calcite-2	−12.0	−0.7	18.5
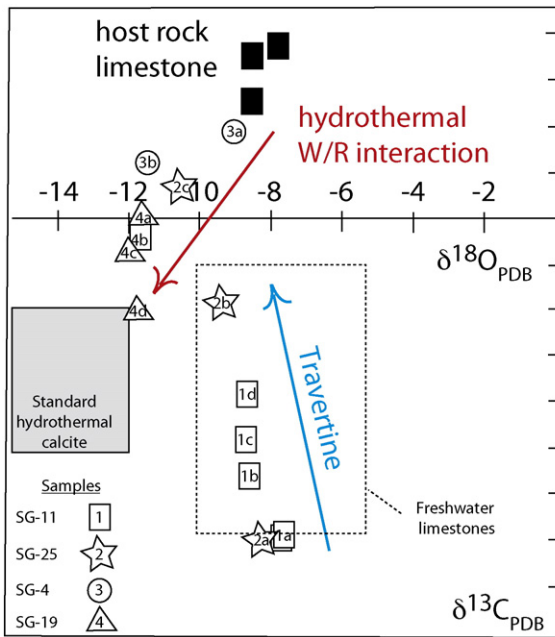
Fig. 6. Carbon and oxygen isotopic values of calcite from the Sierra de Gomez Limestone-hosted U deposit area. The field of standard hydrothermal calcite composition is from Lawton and McMillan (1999). The field for freshwater limestone is from Wilson et al. (1997). a, b, c, and d are sequential microsamples from the limestone to the last chronological cement of each sample.

during thermal maturation of the source rocks before oil generation. Diluted in hydrothermal fluids, these create a corrosion front that increases the intercrystalline and vuggy porosity; this precedes hydrocarbon migration and U-mineralized calcite precipitation.

Hydrothermal fluid is a generic term for hot fluids circulating in the crust; it does not have a genetic implication, and these fluids can be magmatically related or deep, hot basinal brines (Lindgren, 1933). In the Sierra de Gomez mining district, aqueous fluid inclusions range in Th from 86.7 to 112.7 °C, and their salinity ranges from 12.5 to 14.9 wt.% eq $NaCl_{total}$ salinity. No microthermometric data were obtained from the hydrocarbon-bearing monophase fluid inclusions, but Raman spectrometry on these fluid inclusions indicates a composition dominated by ethane for the Type 1 monophase fluid inclusions. The Type 2 two-phase aqueous fluid inclusions have a significant methane concentration, although the two types of fluid inclusions were never

observed in close spatial association. These hydrocarbon occurrences in the Sierra de Gomez mining district, as well as the methane dissolution in the aqueous fluid inclusions and the homogenization temperature and salinity ranges are consistent with descriptions of fluid inclusions for the MVT in the U.S. and northern Mexico (Baldridge et al., 1984; Megaw et al., 1988; Seager et al., 1987; McLemore and North, 1984; Berglof and McLemore, 2003; Martínez-Ibarra et al., 2003; Tritlla et al., 2004; Tritlla et al., 2007). These data also resemble some carbonate oil reservoirs (Seager, 1995; Campos-Enriquez et al., 1999; Martínez-Ibarra et al., 2003). In particular, in the Hansonburg district of the RGR in New Mexico Brune et al. (2014) found that oil from fluid inclusions in fluorite had a salinity ranging from 10 to 17 wt.% NaCl equivalent and a Th ranging from 140 to 205 °C. Fluid inclusions that have oil in fluorite deposits are suggested to be caused by remobilization of organic matter from the sedimentary formations (Averil and Miller, 2013).

The Sierra de Gomez Limestone-hosted U-deposit has a U–Pb date from uranophane of approximately 1.8 Ma. This uranium precipitation age is contemporaneous with the Pliocene Peña Blanca secondary U-mineralization event (from 3.2 to 1.6 Ma; Fig. 7), as well as RGR-type deposits in Chihuahua and intraplate volcanism (Aranda-Gomez et al., 2003; Lueth et al., 2005; Casey, 2011; Angiboust et al., 2012; Figs. 1 and 9). The Sierra de Gomez Limestone-hosted U deposit is contemporaneous with the main regional extensional event of RGR formation from Colorado to the Mexican border. This regional geological scenario suggests the possibility of a favorable extensional context and a thermal anomaly that triggered fluid migration.

Metallogenic models of MVT and RGR-type deposits, including limestone and limestone fault-related U-deposits in the Grant District, are based on the circulation of deep basinal brines that formed from meteoric water dissolution of Jurassic evaporites, with the possible addition of magmatic components (McLemore et al., 1998; McLemore, 2011; Lueth et al., 2005; Megaw et al., 1988). In these models, the reduced basinal brines migrate up to lithological horizons favorable for trapping mineralizing fluids. On the way, they dissolve and alter the wall rock and precipitate various minerals in favorable lithological horizons because of modification of the physical–chemical conditions of the mineralizing fluid, such as adiabatic cooling, mixing, and water/rock interaction (McLemore et al., 1998; McLemore, 2011; Lueth et al., 2005 and references therein).

In the Sierra de Gomez Limestone-hosted U deposit, evidence from local geology, petrography, and stable isotopic values suggests that two main cementation events occurred. The first is related to karst formation and travertine precipitation. The second is the U mineralization

Table 3
Isotopic data for the Sierra de Gomez U-deposit from U–Pb urophane.

| Analysis	Isotopic ratios						Calculated ages (Ma)			
	$^{207}Pb/^{235}U$	Error	$^{206}Pb/^{238}U$	Error	$^{206}Pb/^{207}Pb$	Error	$^{207}Pb/^{235}U$	Error	$^{206}Pb/^{238}U$	Error
Urophane-1	0.00162	0.00065	0.00029	0.00002	0.0516	0.0036	1.6	0.7	1.9	0.1
Urophane-2	0.00169	0.00106	0.00031	0.00003	0.0572	0.0032	1.7	1.1	2	0.2
Urophane-3	0.00234	0.00152	0.00029	0.00003	0.0801	0.0038	2.4	1.5	1.9	0.2
Urophane-4	0.00185	0.00072	0.0003	0.00002	0.0606	0.0016	1.9	0.7	1.9	0.1
Urophane-5	0.0017	0.00042	0.00028	0.00002	0.0561	0.0091	1.7	0.04	1.8	0.1
Urophane-6	0.0019	0.00049	0.00032	0.00005	0.0543	0.0036	1.9	0.5	2	0.4
Urophane-7	0.00175	0.00079	0.00027	0.00002	0.0576	0.0017	1.8	0.7	1.8	0.1
Urophane-8	0.00153	0.00079	0.00027	0.00002	0.0573	0.0015	1.5	0.8	1.7	0.1
Urophane-9	0.00167	0.00123	0.00023	0.00005	0.0661	0.0028	1.7	1.2	1.5	0.3
Urophane-10	0.00194	0.00121	0.00029	0.00011	0.0619	0.0014	2	1.2	1.9	0.7
Urophane-11	0.00193	0.00209	0.00025	0.00004	0.0707	0.0053	2	2.1	1.6	0.3
Urophane-12	0.00235	0.00144	0.00029	0.00004	0.0731	0.0031	2.4	1.5	1.9	0.2
Urophane-13	0.00148	0.00148	0.00028	0.00004	0.0596	0.0034	1.5	1.5	1.8	0.3
Urophane-14	0.00159	0.00034	0.00026	0.00003	0.0584	0.0062	1.6	0.3	1.7	0.2
Urophane-15	0.00159	0.00033	0.00024	0.00002	0.06	0.0089	1.6	0.3	1.6	0.2
Urophane-16	0.00207	0.00064	0.00031	0.00004	0.0586	0.0064	2.1	0.6	2	0.3
Urophane-17	0.00292	0.00108	0.00043	0.00016	0.0588	0.0058	3	1.1	2.8	1.1
Urophane-18	0.00303	0.00105	0.00046	0.00007	0.0571	0.0071	3.1	1.1	3	0.5
Urophane-19	0.00093	0.00071	0.00016	0.00003	0.0567	0.0032	0.9	0.7	1.1	0.2
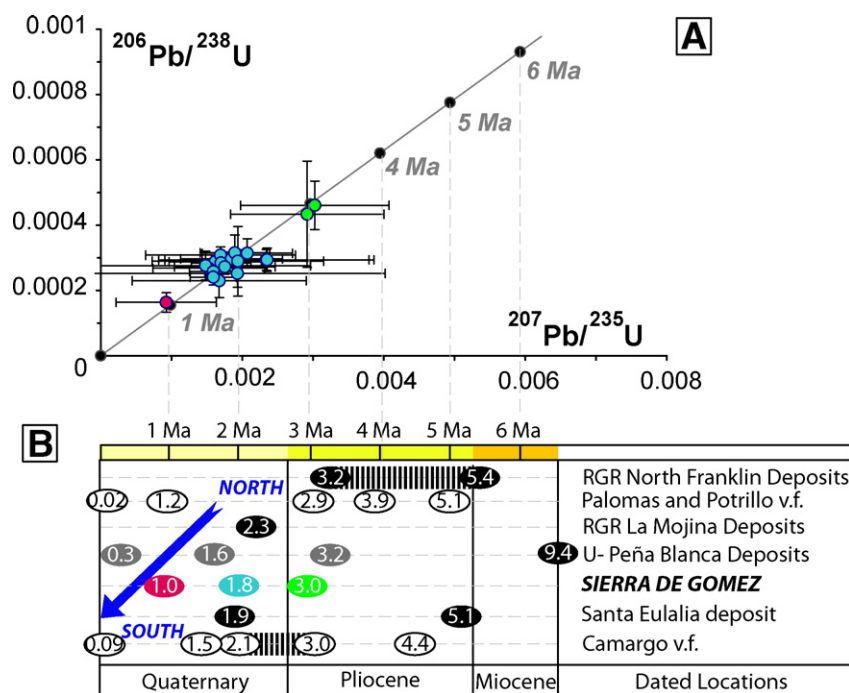
Fig. 7. (A) Concordia diagrams for U–Pb isotopic analysis of uraninite from the Sierra de Gomez U-deposit area. Diagrams, ages, and errors (1s) were generated using the Isoplot 3.71 program (Ludwig, 2008). (B) Compilation of reliable geochronological data available in the state of Chihuahua and southern New Mexico from the Miocene to present (see distribution in Fig. 1), including RGR deposits (Lueth et al., 2005); Peña Blanca deposits (Fayek et al., 2006); the Santa Eulalia deposit (Casey, 2011); the Camargo volcanic field (Aranda-Gomez et al., 2003); and the Potrillo and Palomas volcanic field (Frantes and Hoffer, 1982; Anthony and Poths, 1992; Williams, 2002).

event. The mineralization event begins with corrosion of travertine and Cretaceous limestone, which increased intercrystalline porosity, vug size, and fracture and fault permeability. This corrosion event is favored by the greater reactivity of travertine compared to the dirty Cretaceous limestone. Stable isotopic analysis clearly indicates the hydrothermal nature of the mineralizing fluid and importance of the water/rock interactions. Repetition of the mineralogical succession suggests pulses of hydrothermal activity that are probably related to fault pumping. There is a single type of aqueous fluid inclusions with a restricted range of homogenization temperatures and salinities, suggesting that the precipitation processes involved adiabatic cooling and water rock interactions. The fluid inclusions also highlight the importance of hydrocarbons within the U-mineralizing calcite, which are included as ethane in the crystal growth rims and methane in the aqueous fluid inclusions. The occurrence of hydrocarbons could be a side effect of hydrothermal fluid migration through the Mesozoic sedimentary column, in particular the Late Jurassic series described as the source rock formation (Surdam and Yin, 1994; González and Holguín, 2001). Hydrocarbon occurrence could also be related to hydrothermal fluid interactions with the organic-rich Cretaceous limestone host rock. Water/rock interactions between the U-mineralizing hydrothermal fluid and the organic-rich Cretaceous limestone host rock could liberate hydrocarbon gases and liquids in the hydrothermal system, creating a reducing front that would corrode carbonates and cause mass precipitation of uranium minerals. The occurrence of Cu-, Zn-, Pb-, and Ni-oxidizing minerals within the late paragenesis stage of the Sierra de Gomez Limestone-hosted U-deposit could indicate a relationship with the synchronous RGR-type deposits, which are rich in the same metals (Megaw et al., 1988; McLemore et al., 1998; Lueth et al., 2005). The salinity and metal chemistry of the hydrothermal fluids suggest oxidized meteoric fluids. However, they are channelized to large enough depths to interact with a heat source and cause basement leaching.

Determination of the uranium source is always the most challenging part of creating a metallogenic model. Based on the local geology and the genetic model proposed above, two areas could be involved. The

first is the Placer de Guadalupe horst. The horst structure represents a potential highland for meteoric water recharge and includes Permian/Jurassic and Greenvillian basement outcrops (Villarreal et al., 2014). In addition, various uraninite veins that are Oligocene in age have been described (Krieger, 1932). Finally, the Placer de Guadalupe horst and the Sierra de Gomez are structurally connected (Haenggi, 2002; see Fig. 8). The second possible U source is the Chihuahua Central Graben, which is related to the RGR extension. The Chihuahua Central Graben is filled by Oligocene volcanic rocks and sediments, some of which are enriched in uranium (Mitchell et al., 1981; Goodell, 1981). Uranium-rich underground waters have been identified (Burillo-Montúfar et al., 2012; Reyes-Cortés et al., 2012). The Chihuahua Central Graben is deep enough to generate fluid migration by hydrothermal and/or compaction processes through the RGR extensional faults to a favorable trapping horizon, where uranium could be precipitated by the local generation of a redox barrier created by water/rock interaction processes. Extension and heat anomalies are important regional features of this metallogenetic model. The regional implications of the RGR should be considered to build a more precise model.

6.2. Geometry of the southern Rio Grande rift: implications for the distribution of Quaternary mineral deposits

In northern Chihuahua, the Rio Grande rift is not physiographically distinguishable from the Basin and Range province. Several authors have proposed that the Rio Grande Rift could extend to the Los Muertos basin located in north-central Chihuahua (Baldridge et al., 1984; Lueth et al., 2005; Averil and Miller, 2013); however, the southern extension is not distinct. Various models suggest that the maximum extension of the Rio Grande rift occurs at the Rio Grande River along the border between western Texas and Chihuahua (King and Metcalfe, 2013; among others) and that in New Mexico, RGR emplacement was controlled by its crustal eastern boundary and the position of the thermal anomaly (de Voogd et al., 1986). Geological features that may be related to the Rio Grande rift in Chihuahua were suggested but have never been
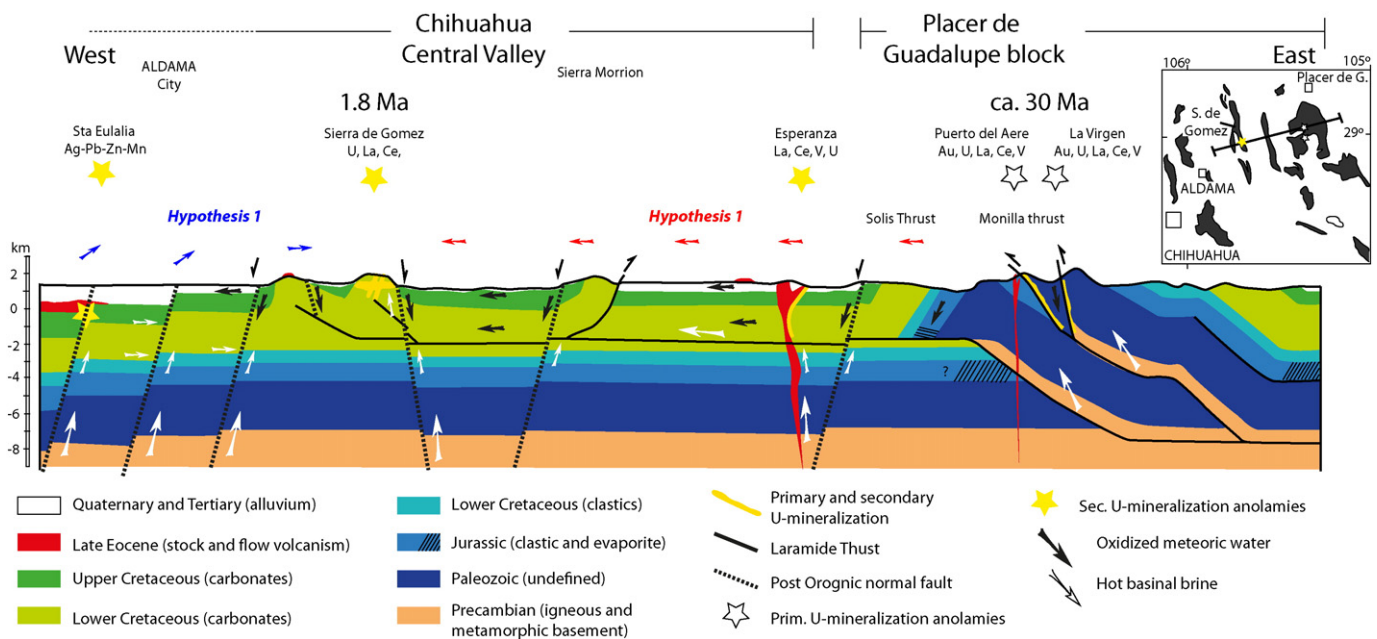
Fig. 8. Schematic genetic model of the Sierra de Gomez Limestone-hosted U deposit (modified from Lueth et al., 2004). Structural transect is taken from Hennings (1994).

placed in the RGR regional geologic context (Fig. 9; Wilson and Rochas, 1948; Lueth et al., 2005; Fayek et al., 2006; Casey, 2011; Angiboust et al., 2012). McLemore (2011) described the genesis of various Pb–F–Ba–Mn mining districts in New Mexico as Rio Grande rift-type deposits (RGR-type; Fig. 9). The detailed characterization is discussed in McLemore et al. (1998) and briefly presented here. Lueth et al. (2005) reported geological and chronological similarities between the La Mojina and Peña Blanca discrete jarosite mineralization events and RGR-type deposits. All deposits are structurally controlled by reactivated N–S trending faults and show a general chronological migration from New Mexico to southern Chihuahua (Fig. 6; Wilson and Rochas, 1948; Lueth et al., 2005; Angiboust et al., 2012). Plio-Quaternary volcanism outcrops in Chihuahua have been noted in the Camargo volcanic field (Figs. 1 and 9; Aranda-Gomez et al., 2003; Fayek et al., 2006) and in the Mexico–U.S. transborder Palomas and Potrillo volcanic fields (Hofer, 1976; Frantes and Hoffer, 1982; Williams, 2002; Fayek et al., 2006; Aranda-Gómez et al., 2007; Munjea et al., 2014; Munjea et al., 2014). The volcanism has been characterized as an intraplate mafic alkalic volcanic series that is Pliocene-Pleistocene in age and strongly controlled by northwest-striking normal faulting (approximately 5 to 0.09 Ma in age; Fig. 4B; Hawley, 1981; Morgan et al., 1998; Anthony and Poths, 1992; Aranda-Gomez et al., 2003; Munjea et al., 2014). Metallogenic and volcanic events and graben filling are the oldest known events. Metallogenic and volcanic events can be divided into at least three periods coeval with extension, which occurred at approximately 5 Ma and 3 Ma and between 2 Ma and present (Fig. 7). All of the metallogenic and volcanic occurrences are distributed along the Chihuahua Central Graben. The grabens in western and central Chihuahua are at least Eocene in age and exhibit a variety of sedimentary fills until the present. Along the west Texas border, volcanism has been absent since the early Miocene (Dickerson and Muehlberger, 1994), and the mineral deposits that have been described are Tertiary in age (Mclemore et al., 1998; James and Henry, 1993). Incorporation of the Peña-Blanca and Sierra de Gomez U-deposits in the RGR deposit chronology creates a continuum along a common geomorphologic structure, the Chihuahua Central Graben, that spans the La Mojina deposit, located south of the Los Muertos basin, the Santa Eulalia deposit, and the Camargo volcanic field south of the state of Chihuahua. Mineral deposits, volcanic occurrences, and regional hydrothermal anomalies

imply not only extension but also the presence of crustal fractures that facilitated effective fluid circulation. The restricted area and time emplacement of these mineral deposits and volcanic fields, which only occur along the Chihuahua Central Graben and are far from the present RGR basin along the Rio Bravo River, highlight a probable genetic relationship. The oldest RGR basin, the Tornillo basin, includes a sedimentary record of vertebrates from the late Miocene (11–9 Ma; Stevens and Stevens, 1990) to the present.

Various geological features could also represent indicators of thermal activity and extension. Among these, we focus on historical seismicity (Fig. 6; 1900 to present; Suter, 2001; Galván-Ramírez and Montalvo-Arrieta, 2008; Morton and Bilek, 2014) and the location of medium to high enthalpy geothermal spots (Iglesias et al., 2011). The medium to high enthalpy geothermal spot locations indicate present anomalous heat flow and deep-rooted channels of actual thermal fluid circulation. These spots could be interpreted as the modern, shallow expression of RGR paleohydrothermal mineral deposits. It is important to note that none of the geothermal spot locations are spatially related to the Plio-Quaternary volcanism outcrops. The higher enthalpy geothermal spot locations are related to the N–S extensional faults in the southern part of central Chihuahua. The historical seismicity has a low intensity level (with magnitudes below 3) and has been interpreted to indicate extensional components along NNW–SSE crustal fractures (20 to 3 km depth; Doser and Rodriguez, 1993; Galván-Ramírez and Montalvo-Arrieta, 2008. The geothermal spots and seismicity occur in two main geographic areas: (1) to the west, overlapping the metallogenic and volcanic districts along the Chihuahua Central Graben and the western limit of the Chihuahua trough (Figs. 9 and 10), and (2) to the east, along the Rio Grande River basin and overlapping the area of maximum thickness of Jurassic evaporites. Both areas converge at the southern extension of the Los Muertos basin (Figs. 9 and 10) north of the Plomosa uplift.

The distribution of Mio-Pliocene to Quaternary extension proxies from central to western Chihuahua is contemporaneous with the formation of the RGR. The evolution of extension is coherent with northward migration of the RGR thermal anomaly. From the late Miocene to the present, the extension affected large areas of the state of Chihuahua, and all grabens from the Chihuahua Central Graben to the Rio Grande River Basin exhibit continuous extension. However, to the west (in the
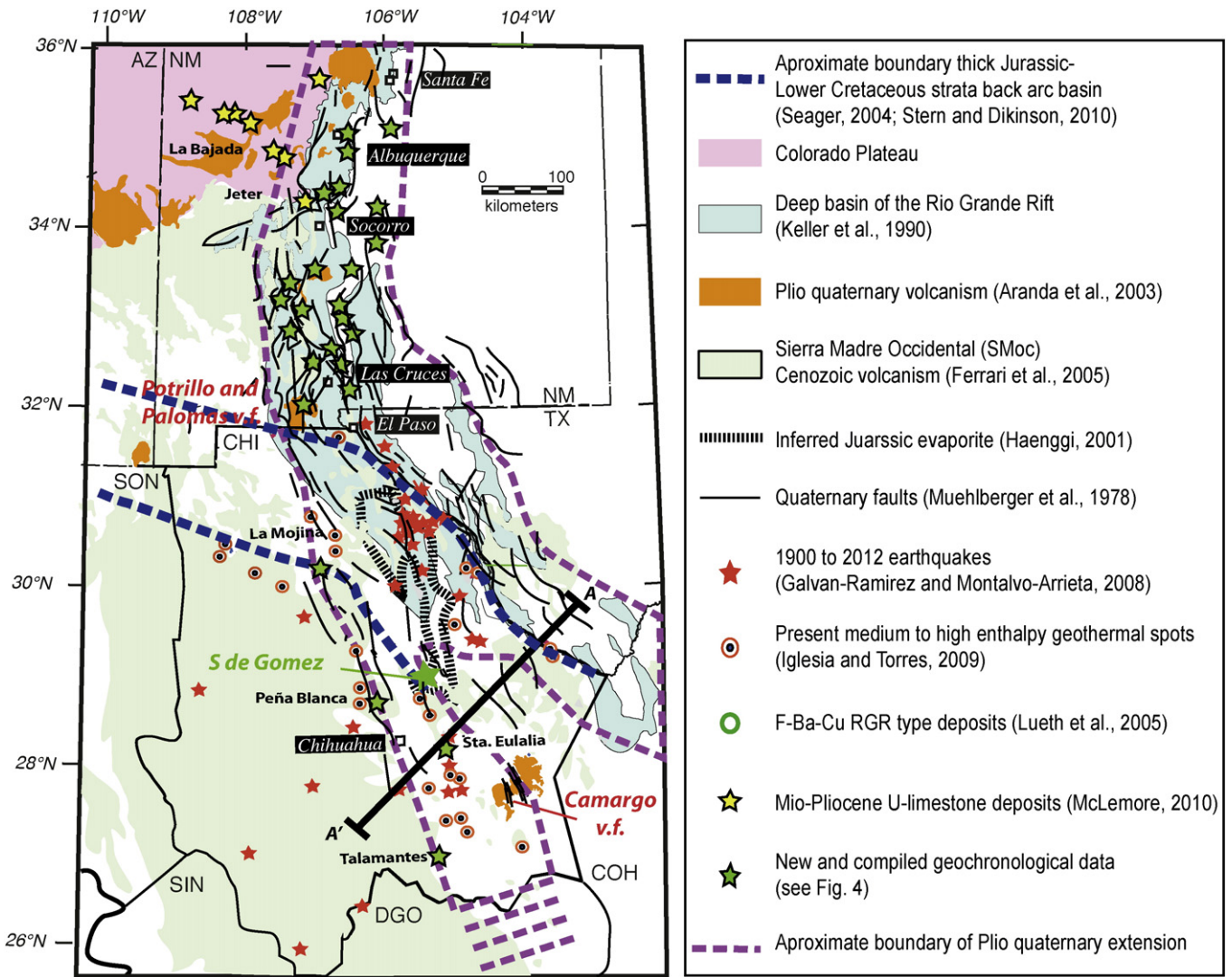
Fig. 9. (A) Map showing the distributions of various geological proxies for extension along the Chihuahua Central Valley and the Rio Bravo River, as well as the migration of extension from west to east and its actual distribution. Brown dotted line highlights the area affected by Mio-Pliocene to Quaternary extension in Chihuahua: (1) Mio-Pliocene extension events; and (2) present extension event.

Chihuahua Central Graben), the asthenospheric anomaly is more intense, and the structures inherited from the Basin and Range event are deeper. They have high angles and deep roots that still allow magmatic intrusion and hydrothermal cell development. To the East, the extensional style is thin skin tectonics controlled by the inherited listric fault to the east (de Voogd et al., 1986). The eastern area is far enough from the asthenospheric anomaly to remain unaffected by the present and past hydrothermal and volcanic activity. Between these two major structures, the present pattern of seismicity suggests that deformation is accommodated within the Jurassic basin by the evaporite horizon. Regional uplift and doming usually result when a continent comes to rest over asthenospheric uplift. Extensional failure of the lithospheric crust may occur with continued doming, triggering the development of a triple junction, or a three-armed continental rift system. Typically, one arm of the rift fails and thus remains a fissure in the crust, which is known as an aulacogen; in contrast, the remaining two open arms eventually form an oceanic basin. This triple junction geometry is controlled by the heterogeneity of the continental crust and the tensions that allow accommodation of the displacements (Jolivet et al., 1994; Yoon et al., 2014; Brune et al., 2014). Brune et al. (2014) performed rift modeling and highlighted that a large-scale asymmetry does not form when a single large detachment fault cross cuts the crust; rather, such asymmetry is the result of an array of dipping faults

acting sequentially in time. These faults are gradually abandoned as the central rift migrates to the side. The initial thermal profile and the crustal thickness and structure, as well as the extension velocity, are the key factors controlling the asymmetry of rift geometry (Brune et al., 2014).

We note several observations based on the tectonic map of the state of Chihuahua and the Chihuahua Central Graben. The border rift system in Chihuahua is intimately associated with the Nazas magmatic arc and the Chihuahua Trough sedimentary transgression during Kimmeridgian time (156–151 Ma; Dickinson and Lawton, 2001b). The late Jurassic basin continuum, including the Bisbee basin, the Chihuahua basin, and the Sabinas basin, intersects near the southern region of the Rio Grande at archetypal angles of approximately 120°, in what Stern and Dickinson (2010) call the Rio Grande triple junction. The Rio Grande rift propagation is thus under the influence of two large-scale phenomena: (1) "classical" asthenospheric uplift, which provides the extensional component, and (2) a complex geodynamic history that is the sum of Permo-Jurassic back arc formation, Cordilleran orogeny and Basin and Range collapse.

The distributions of the Plio-Quaternary mineral deposits and modern low to medium enthalpy hydrothermal spots are clear evidence that during Chihuahua's geological history, some major crustal structures were reactivated and thus influenced its geological evolution, including the complex Rio Grande triple junction. Some of these structures could
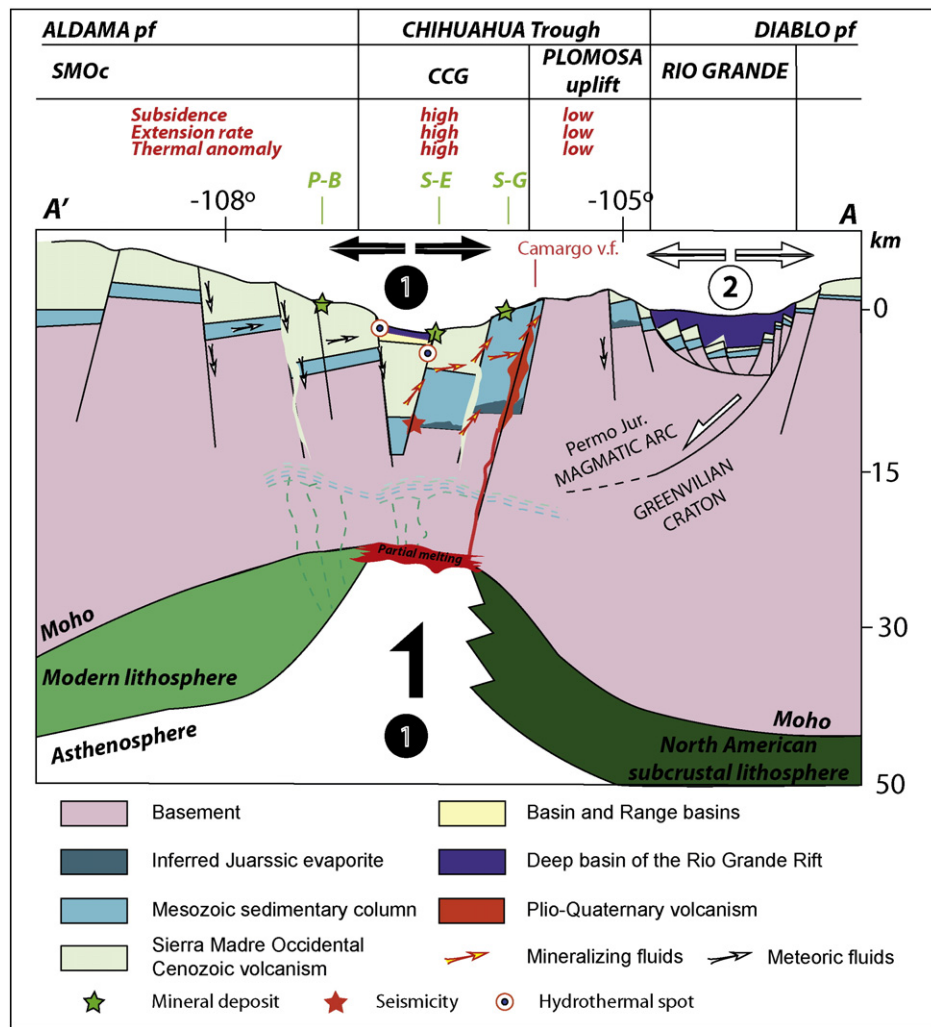
Fig. 10. Schematic crustal cross-section of southern Chihuahua. Cross section is based on de Voogd et al. (1986), Olsen et al. (1987), Russel and Snelson (1994), and Levander et al. (2011), and McLemore (1999) and (2011). Green stars indicate the location of mineral deposits. P-B: Peña Blanca U–Mn deposit, S-G: Sierra de Gomez U-deposit, S-E: Santa Eulalia Ag–Pb–Zn–Mn deposit, SMOc: Sierra Madre Occidental, CCG: Chihuahua Central Graben.

be the Chihuahua Central Graben, the Plomosa uplift and the RGR's eastern boundary. The Basin and Range structure, formation of Jurassic basins, Jurassic arc accretion structures, and asthenospheric uplift are all characteristics that influenced the large-scale development and central migration of the Rio Grande rift. This geological evolution restricts the potential distribution of the redistributed and limestone-associated U-anomalies within the extended area of the Rio Grande rift.

The Chihuahua Central Graben and nearby areas provide the three necessary conditions for uranium enrichment of limestone deposits: (1) a source, in this case, uranium-rich Oligocene volcanism and/or basement; (2) an efficient transport mechanism for large-scale input of oxidized meteoritic waters, which were channeled into deep extensional Plio-Quaternary reactivated structures and supported by large thermal anomalies and sedimentary compaction processes; and (3) an effective trap, which here is the generation of a redox front by water/rock processes between oxidized hydrothermal mineralizing fluids ascending along the deep reactivated structures of the RGR and organic matter-rich Cretaceous limestones.

7. Conclusions

The Sierra de Gomez is a limestone uranium deposit that is 1.8 Ma in age. It is contemporaneous to the Peña Blanca U-deposits; the Santa Eulalia jarosite alteration; RGR and uranium deposits in New Mexico and Chihuahua; and the Paloma, Potrillo, and Camargo intraplate volcanic fields. The Sierra de Gomez limestone U-deposit is formed by a local redox front generated by direct interaction between organic matter-rich limestone and hydrothermal sedimentary brine, which caused channeling in long, deep Plio-Quaternary extensional structures. We have reviewed some of the geological and chronological evidence of extension in Chihuahua from the Plio-Quaternary to the present. The oldest extension occurred rapidly and is related to the Basin and Range area. The distribution of Mesozoic sedimentary facies, Plio-Quaternary mineral deposits, modern seismicity and low to medium enthalpy hydrothermal spots, and the sedimentary fills give clear evidence that the Chihuahua Central Graben represents a major crustal structure that was reactivated many times between the early Mesozoic and the present. The last reactivation event of the Chihuahua Central Graben is contemporaneous with RGR development. The Chihuahua Central Graben accommodated the RGR extension before it be extended to the east. The Chihuahua Central Graben presents intense heat anomalies and a high capacity for expulsion of hot fluids, and thus is likely the source of the U-mineralizing fluids forming the Sierra de Gomez Limestone-hosted U deposit.

References

Angiboust, S., Fayek, M., Power, I., Camacho, A., Calas, G., Southam, G., 2012. Structural and biological control of the Cenozoic epithermal uranium concentrations from the Sierra Peña Blanca, Mexico. Mineral. Deposita 47, 859–874.

Anthony, E.Y., Poths, J., 1992. [3]He surface exposure dating and its implications for magma evolution in the Potrillo Volcanic Field, Rio Grande rift, New Mexico, USA. Geochim. Cosmochim. Acta 56, 4105–4108.

Aranda-Gomez, J.J., Luhr, J.H., Housh, T.B., Connor, C.B., 2003. Synextensional Pliocene–Pleistocene eruptive activity in the Camargo volcanic field, Chihuahua, Mexico. Geol. Soc. Am. Bull. 115, 298–313.

Aranda-Gómez, J.J., Molina-Garza, R., McDowell, F.W., Vasallo-Morales, L.F., Ortega-Rivera, M.A., Solorio-Munguía, J.G., Aguillón-Robles, A., 2007. The relationships between volcanism and extension in the Mesa Central: the case of Pinos Zacatecas, Mexico. Rev. Mex. Cienc. Geol. 24, 216–233.

Averil, M.G., Miller, K.C., 2013. Upper crustal structure of the southern Rio Grande rift: a composite record of the rift and pre rift tectonic. Geol. Soc. Am. Spec. Pap. 494, 463–474.

Baldridge, W.S., 2004. Geology of the America Southwest: A Journey Through Two Billion Years of Plate Tectonic History. Cambridge University Press, p. 314.

Baldridge, W.S., Olsen, K.H., Callender, J.F., 1984. Rio Grande rift: problems and perspectives. New Mexico Geological Society Guidebook, 35th Field Conference, Rio Grande Rift: Northern New Mexico.

Bartolino, J.R., 1992. Modified basin and range topography in the Bolson de Mapimi, Durango and Chihuahua, Mexico. Tex. J. Sci. 44, 295–300.

Berglof, W.R., McLemore, V.T., 2003. Economic geology of the Todilto Formation. New Mexico Geological Society 54th Annual Fall Field Conference Guidebook, pp. 179–189.

Brune, S., Heine, C., Perez-Gussinyé, M., Sobolev, S.V., 2014. Rift migration explains continental margin asymmetry and crustal hyper-extension. Nature 1-9.

Burillo-Montúfar, J.C., Reyes Cortés, M., Reyes Cortés, I.A., Espino Valdez, M.S., Hinojosa de la Garza, O.R., Nevárez Ronquillo, D.P., Herrera Peraza, E., Rentería Villalobos, M., Montero Cabrera, M.E., 2012. Uranium-series isotopes transport in surface, vadose and ground waters at San Marcos uranium bearing basin, Chihuahua, Mexico. Appl. Geochem. 27, 1111–1122.

Cameron, K.L., Nimz, G.J., Niemeyer, S., Gunn, S., 1989. Southern Cordilleran basaltic andesite suite, southern Chihuahua, Mexico: a link between Tertiary continental arc and flood basalt magmatism in North America. J. Geophys. Res. 94 (B6), 7817–7840.

Campos-Enriquez, J.O., Ortega-Ramirez, J., Alatriste-Vilchis, D., Cruz-Gatica, R., Cabral-Cano, E., 1999. Relationship between extensional tectonic style and the paleoclimatic elements at Laguna El Fresnel, Chihuahua desert, Mexico. Geomorphology 28, 75–94.

Casey, H., 2011. Geochemistry of manganese oxides and age of mineralization at Santa Eulalia mining district, Mexico (PhD dissertation) New Mexico Institute of Minning and Technology, p. 137.

Cawood, P.A., Hawkesworth, C., 2013. Temporal relations between mineral deposits and global tectonic cycles. In: Jenkin, G.R.T., Lusty, P.A.J., McDonald, I., Smith, M.P., Boyce, A.J., Wilkinson, A.J. (Eds.), Ore Deposits in an Evolving EarthGeol. Soc. Spec. Pub. 393. Geological Society, London.

Chapin, C.E., Wilks, M., McIntosh, W.C., 2004. Space–time patterns of Late Cretaceous to present magmatism in New Mexico—comparison with Andean volcanism and potential for future volcanism. Bur. Geol. Min. Res Bull. 160, 13–39.

Cosca, M.A., Thompson, R.A., Lee, J.P., Turner, K.J., Neymark, L.A., Premo, W.R., 2014. [40]Ar/[39]Ar geochronology, isotope geochemistry (Sr, Nd, Pb), and petrology of alkaline lavas near Yampa, Colorado: migration of alkaline volcanism and evolution of the northern Rio Grande rift. Geosphere 10, 1–27.

Cuney, M., 2009. The extreme diversity of uranium deposits. Mineral. Deposita 44, 3–9.

Cuney, M., 2010. Evolution of uranium fractionation processes through time: driving the secular variation of uranium deposit types. Econ. Geol. 105, 553–569.

De Voogd, B., Brown, L.D., Merey, C., 1986. Nature of the Eastern Boundary of the Rio Grande rift from COCORP surrey in the Albuquerque basin, New Mexico. J. Geophys. Res. 91, 6305–6320.

DeAngelo, M.V., Keller, G.R., 1988. Geophysical anomalies in southwestern New Mexico. In: G.H., M., T.F., L., S.G., L. (Eds.), Cretaceous and Laramide Tectonic Evolution of Southwestern New Mexico. New Mexico Geological Society, Guidebook 39, pp. 71–75.

Dickerson, P.W., Muehlberger, W.R., 1994. Basins in the Big Ben segment of the Rio Grande rift, Trans Pecos Texas. Geol. Soc. Am. Spec. Pap. 291, 283–297.

Dickinson, W.R., Lawton, T.F., 2001b. Tectonic setting and sandstone petrofacies of the Bisbee basin (USA–Mexico). J. S. Am. Earth Sci. 14, 475–504.

Doser, D.I., Rodriguez, J., 1993. The seismicity of Chihuahua, Mexico, and the 1928 Parral earthquake. Phys. Earth Planet. Inter. 78, 97–104.

Easley, E., Garchar, L., Bennett, M., Beasley, B., Woolf, R., Hoopes, J., 2011. Investigation of geothermal resource potential in the northern Rio Grande rift, Colorado and New Mexico. Geotherm. Resour. Counc. Trans. 35, 761–768.

Ewing, E.E., 2013. Subsidence and uplift history of the West Texas Basin and its (post-Paleozoic) margins. AAPG, Search and Discovery Article #30272.

Fayek, M., Ren, M., Goodell, P., Dobson, P., Saucedo, A.L., Kelts, A., Utsunomiya, S., Ewing, R.C., Riciputi, L.R., Reyes, I., 2006. Paragenesis and geochronology of the Nopal I uranium deposit, Mexico. 11th International High Level Radioactive Waste Management Conference Proceeding, Las Vegas, NV, pp. 55–62.

Ferrari, L., Valencia-Moreno, M., Bryan, S., 2005. Magmatismo y tectónica en la Sierra Madre Occidental y su relación con la evolución de la margen occidental de Norteamérica. Bol. Soc. Geol. Mex. LVII, 343–378.

Frantes, T.J., Hoffer, J.M., 1982. Palomas volcanic field, southern New Mexico and northern Chihuahua: New Mexico. Geology 4 (6–8), 16.

Galván–Ramírez, I.N., Montalvo–Arrieta, J.C., 2008. The historical seismicity and prediction of ground motion in northeast Mexico. J. S. Am. Earth Sci. 25, 37–48.

Goldstein, R.H., Anderson, J.E., Bowman, M.W., 2010. Diagenetic responses to sea-level change: integration of field, stable isotope, paleosol, fluid inclusion, and cement stratigraphy research to determine history and magnitude of sea-level fluctuation. Kans. Geol. Surv. Bull. 233, 139–162.

González, G.R.N., Holguín, Q., 2001. Las rocas generadoras de México. Bol. AMGP XLIX (1–2), 16–30.

Goodell, P.C., 1981. Geology of the Peña Blanca uranium deposits, Chihuahua, Mexico. In: P.C., G., Waters, A. (Eds.), Uranium in Volcanic and Volcanoclastic Rocks. AAPG El Paso 13, pp. 275–291.

Haenggi, W.T., 2001. Tectonic history of the Chihuahua trough, Mexico and adjacent USA, part I: the pre-Mesozoic setting. Bol. Soc. Geol. Mex. LIV, 28–66.

Haenggi, W.T., 2002. Tectonic history of the Chihuahua trough, Mexico and adjacent USA, part II: Mesozoic and Cenozoic. Bol. Soc. Geol. Mex. LV (1), 38–94.

Hawley, J.W., 1981. Pleistocene and Pliocene history of the international boundary area, southern New Mexico Northern. Geology of the Border, Southern New Mexico–Northern Chihuahua. El Paso Geological Society, Field Trip Guidebook, pp. 26–32.

Hennings, P.H., 1994. Structural transect of the southern Chihuahua fold belt between Ojinaga and Aldama, Chihuahua, Mexico. Tectonics 13, 1445–1460.

Hofer, J.M., 1976. Late Cenozoic Basalt of the Southern Rio Grande Rift, Southern New Mexico, West Texas, and Northern Chihuahua, Mexico. Abstracts of Papers Presented to the Conference on Processes of Planetary Rifting. A Lunar and Planetary Institute Topical Conference Held December 3–5.

Hudson, M.R., Grauch, V.J.S., 2013. Introduction. In: Hudson, M.R., Grauch, V.J.S. (Eds.), New Perspectives on Rio Grande Rift Basins: From Tectonics to Groundwater. Geol. Soc. Am. Spec. Paper 494, pp. v–xii.

Iglesias, E.R., Torres, R.J., Martínez-Estrella, J.I., Reyes-Picasso, N., 2011. Resumen de la evaluación 2010 de los recursos geotérmicos mexicanos de temperatura intermedia a baja. Geotermia 24, 2, 39–48.

James, E.W., Henry, C.D., 1993. Pb isotopes of ore deposits in Trans-Pecos Texas and northeastern Chihuahua, Mexico; basement, igneous, and sedimentary sources of metals. Econ. Geol. 88, 934–947.

Jolivet, L., Tamaki, K., Fournier, M., 1994. Japan Sea, opening history and mechanism: a synthesis. J. Geophys. Res. 99 (B11), 22,237–22,259.

Keller, G.R., Baldridge, S.W., 1999. The Río Grande rift: a geological and geophysical overview. Rocky Mt. Geol. 34 (1), 121–130.

Keller, G.R., Cather, S.M., 1994. Introduction. In: Keller, G.R., Cather, S.M. (Eds.), Basins of the Rio Grande Rift: Structure, Stratigraphy, and Tectonic Setting. Geol. Soc. Am. Spec. Paper 291, p. 304.

Keller, G.R., Khan, M.A., Morgan, P., Wendlandt, R.F., Baldridge, W.S., Olsen, K.H., Prodehl, C., Braile, L.W., 1991. A comparative study of the Rio Grande and Kenya rifts. Tectonophysics 197, 355–371.

King, D., Metcalfe, E., 2013. Rift zones as a case study for advancing geothermal occurrence models. Proceedings, 38th Workshop on Geothermal Reservoir Engineering, Stanford University, Stanford, California, February 11–13.

Koptev, A., Calais, E., Burov, E., Leroy, S., Gerya, T., 2015. Dual continental rift systems generated by plume–lithosphere interaction. Nature 8, 388–392.

Krieger, P., 1932. An association of gold and uraninite from Chihuahua, Mexico. Econ. Geol. 27, 651–660.

Lara-Zavala, J., 1960. Estudio sobre los yacimientos de minerales radioactivos de la sierra de Gómez, Municipio de Aldama, Estado de Chihuahua. U.N.A.M., Facultad de Ingeniería (61 pp.).

Lawton, T.F., McMillan, N.J., 1999. Arc abandonment as a cause for passive continental rifting: comparison of the Jurassic Mexican Borderland rift and the Cenozoic Rio Grande rift. Geology 27, 779–782.

Levander, A., Schmandt, B., Miller, M.S., Liu, K., Karlstrom, K.E., Crow, R.S., Lee, C.T.A., Humphreys, E.D., 2011. Continuing Colorado plateau uplift by delamination-style convective lithospheric downwelling. Nature 472, 461–466.

Lindgren, W., 1933. Mineral Deposits. fourth ed. McGraw-Hill.

Ludwig, 2008. Isoplot/EX Version 3.0, A Geochronological Toolkit for Microsoft Excel. Berkeley Geochronology Center Special Publication.

Lueth, V.W., Rye, R.O., Peters, L., 2005. "Sour gas" hydrothermal jarosite: ancient to modern acid-sulfate mineralization in the southern Rio Grande rift. Chem. Geol. 215, 339–360.

Lueth, V.W., Chamberlin, R.M., Peters, L., 2004. Age of mineralization in the Luis Lopez manganese district, Socorro County, New Mexico, as determined by [40]Ar/[39]Ar dating of cryptomelane. Bull. New Mex. Bur. Min. Mineral Resour. 160, 239–249.

Martínez-Ibarra, R., Tritlla, J., Cedillo-Pardo, E., Grajales-Nishimura, J.M., Murillo-Muñetón, G., 2003. Brine and hydrocarbon evolution during the filling of the Cantarell Oil Field (Gulf of Mexico). J. Geochem. Explor. 78–79, 399–403.

Mauger, R.L., McDowell, F.W., Blount J.G., 1983. Grenville-age Precambrian rocks of the Los Filtros area near Aldama, Chihuahua, Mexico: In Geology and Mineral Resources of North-Central Mexico, K.F. Clark and P.C. Goodell, eds. El Paso Geological Society, Field Conference Guidebook, 165–168.

McCrea, J.M., 1950. On the isotopic chemistry of carbonates and a paleotemperature scale. J. Chem. Phys. 18, 849–857.

McDowell, F.W., Roldán-Quintana, J., Amaya-Martínez, 1997. Interrelationship of sedimentary and volcanic deposits associated with Tertiary extension in Sonora, Mexico. Geol. Soc. Am. Bull. 109, 1349–1360.

McLemore, V.T., 1999. La Bajada uranium-base-metal deposit, Santa Fe County, New Mexico. New Mexico Geological Society 50th Annual Fall Field Conference Guidebook, pp. 445–448.

McLemore, V.T., 2011. The Grants Uranium District, New Mexico: update on source, deposition, and exploration. Mt. Geol. 48 (1), 23–44.
McLemore, V.T., North, R.M., 1984. Occurrences of precious metals and uranium along the Rio Grande rift in northern New Mexico. In: Baldridge, W.S., Dickerson, P.W., Riecker, R.E., Zidek, J. (Eds.), Rio Grande Rift (Northern New Mexico). New Mexico Geological Society 35th Annual Fall Field Conference Guidebook, pp. 205–212.
McLemore, V.T., Donahue, K., Krueger, C.B., Rowe, A., Ulbricht, L., Jackson, M.J., Breese, M.R., Jones, G., Wilks, M., 2002. Data-base of the uranium mines, deposits, occurrences, and mills in New Mexico. New Mexico Bureau of Geology and Mineral Resources Open-File Report. 461 (CD-ROM: http://geoinfo.nmt.edu/publications/openfile/details.cfml?Volume=461 (accessed December 8, 2010)).
McLemore, V.T., Giordano, T.H., Lueth, V.W., Witcher, J.C., 1998. Origin of barite–fluorite–galena deposits in the southern Rio Grande rift, New Mexico. Guideb. N. M. Geol. Soc. 49, 251–263.
Megaw, P.K.M., Ruiz, J., Titley, S.R., 1988. High-temperature, carbonate-hosted Ag–Pb–Zn(Cu) deposits of northern Mexico. Econ. Geol. 83, 1856–1885.
Mitchell, S., Goodell, P.C., LeMone, D.V., Pingitore, N.E., 1981. The geology of the Sierra Gomez, Chihuahua, Mexico. Studies in Geology #13. Amer Assoc. Petrol. Geol., pp. 293–310.
Goteti, R., Mitra, G., 2013. Three-dimensional finite-element modeling of fault interactions in rift-scale normal fault systems: implications for the late Cenozoic Rio Grande rift of north-central New Mexico. Geol. Soc. Am. Spec. Pap. 494, 157–184.
Morgan, G.S., Lucas, S.G., Mack, G.H., 1998. Pliocene (Blancan) vertebrate fossils from the Camp Rice Formation near Tonuco Mountain, Dona Ana County, southern New Mexico. N. M. Geol. Soc. Guideb. 49, 237–249.
Morton, E.A., Bilek, S.L., 2014. Limited dynamic earthquake triggering in the Socorro Magma Body Region, Rio Grande rift, New Mexico. Bull. Seismol. Soc. Am. 104 (5), 2182–2193.
Munjea, P., Haemyeong, J., Yougwoo, K., 2014. Petrofabrics of olivine in a rift axis and rift shoulder and their implications for seismic anisotropy beneath the Rio Grande rift. Island Arc 23, 299–311.
Nandigam, R., Clark, K.F., Anthony, E.Y., Comaduran-Ahumada, O., 2009. Características geológicas y geoquímicas de un complejo carbonatítico enriquecido en Zn y LREE del Terciario de Chihuahua septentrional, México. In: Clark, K.F., Salas-Pizá, G.A., Cubillas-Estrada, R. (Eds.), Geologia Económica de Mexico, second ed. Asociación de Ingenieros de Minas, Metalurgistas y Geólogos de México, Servicio Geológico Mexicano, pp. 506–516.
Oakes, C.S., Bodnar, R.J., Simonson, J.M., 1990. The system NaCl–CaCl$_2$–H$_2$O: the ice liquidus at 1 atm total pressure. Geochim. Cosmochim. Acta 54, 603–610.
Olsen, K.H., Baldridge, W.S., Callender, J.F., 1987. Rio Grande rift: an overview. Tectonophysics 143, 119–139.
Ortega-Ramirez, J.J., Maillol, M., Urrutia-Fucugauchi, J., Valiente-Banuet, A., Bandy, W., Martinez-Serrano, R., 2001. Tectonic and climate change controls in late Quaternary alluvial-fan development in the Playa El Fresnal region, north Chihuahuan desert, Mexico. Arid Land Stud. 11 (3), 142–158.
Oviedo-Patron, E.G., Aranda-Gomez, J.J., Chavez-Cabello, G., Milona-Garza, R.S., Iriondo, A., Gonzalez-Becerra, P.C., Cervantes-Corona, J.A., Solorio-Munguia, J.G., 2010. Tectónica de la sierra Cuesta El Infierno y su posible relación con fallas reactivadas cerca del levantamiento de Plomosas, Chihuahua, México. Rev. Mex. Cienc. Geol. 27 (3), 389–411.
Ragnarsdottir, K.V., Charlet, L., 2000. Uranium behaviour in natural environments. In: Cotter-Howells, J., Batchelder, M., Campbell, L., Valsami-Jones, E. (Eds.), Environmental Mineralogy: Microbial Interactions, Antropogenic Influences, Contaminated Lands and Waste Management. Mineral. Soc. of GB, pp. 333–377.
Reiter, M., Tovar, R.J.C., 1982. Estimates of terrestrial heat flow in northern Chihuahua, based upon petroleum bottom hole temperatures. GSA Bull. 93, 613–624.
Reyes-Cortés, M., Reyes-Cortés, I.A., Espino-Valdez, S., Rentería-Villalobos, M., Burillo-Montúfar, J.C., Montero-Cabrera, M.E., 2012. Origen and distribution of the natural radioactivity in the northern part of the Chihuahua basin, Mexico. Rev. Mex. Cienc. Geol. 29, 659–675.
Russel, L.R., Snelson, S., 1994. Structure and tectonics of the Albuquerque Basin segment of the Rio Grande rift: insights from reflection seismic data. In: Keller, G.R., Cather, S.M. (Eds.), Basins of the Rio Grande Rift: Structure, Stratigraphy, and Tectonic Setting. Geol. Soc. Am. Spec. Paper 291, pp. 83–112.
Seager, W.R., 1981. Geology of the organ mountains and southern San Andres Mountains, New Mexico. New Mex. Bur. Min. Mineral Resour. Mem. 36 97 pp.
Seager, W.R., 1995. Geologic map of the southwest quarter of the Las Cruces and northwest part of the El Paso 1° × 2° sheets. New Mexico Bureau of Mines and Mineral Resources, Geologic Map 60, Scale 1:125,000.
Seager, W.R., Hawley, J.W., Kottlowski, F.E., Kelley, S.A., 1987. Geology of east half of Las Cruces and northeast El Paso 1° × 2° sheets, New Mexico. New Mexico Bureau of Mines and Mineral Resources, Geologic Map. 57.
Stern, R.J., Dickinson, W.R., 2010. The Gulf of Mexico is a Jurassic backarc basin. Geosphere 6, 739–754.
Stevens, J.B., Stevens, M.S., 1990. Road logs, field trip to Big Bend region, Trans-Pecos Texas. In: Dickerson, P.W., Stevens, M.S., Stevens, J.B. (Eds.), Geology of the Big Bend and Trans-Pecos Region. South Texas Geological Society, 1989 Annual Meeting of American Association of Petroleum Geologists, Field Trip Guidebook, pp. 1–72.
Surdam, R.C., Yin, P., 1994. Organic acids and carbonate stability, the key to predicting positive porosity anomalies. In: Pittman, E.D., Lewan, M.D. (Eds.), Organic Acids in Geological Processes. Springer-Verlag, Berlin (482 pp.).
Suter, M., 2001. The historical seismicity of northeastern Sonora and northwestern Chihuahua, Mexico (28–32° N, 106–111° W). J. S. Am. Earth Sci. 14, 521–532.
Torres, R., Ruiz, J., Patchett, P.J., Grajales, J.M., 1999. Permo-Triassic continental arc in eastern México: tectonic implications for reconstructions of southern North America. In: Bartolini, C., Wilson, J.L., Lawton, T.F. (Eds.), Mesozoic Sedimentary and Tectonic History of North-Central Mexico. Geol. Soc. Am. Spec. Paper 340, pp. 191–196.
Tritlla, J., González-Partida, E., Levresse, G., Banks, D., Pironon, J., 2004. Fluorite deposits at Encantada-Buenavista, Mexico: products of Mississippi Valley type processes [Ore Geol. Rev. 23 (2003), 107–124] — a reply. Ore Geol. Rev. 25, 329–332.
Tritlla, J., Levresse, G., Corona-Esquivel, R., Banks, D.A., Lamadrid, H., 2007. Epigenetic, low-temperature, carbonate-hosted Pb–Zn–Cu–Ba–F–Sr deposits in México: a Mississippi Valley–type classification. In: Alanis-Alvarez, S.A., Nieto-Samaniego, A.F. (Eds.), Geology of México: Celebrating the Centenary of the Geological Society of Mexico. Geological Society of America Special Paper 422, pp. 417–432.
Villarreal, J., Levresse, G., Nieto-Samaniego, A., Corona-Esquivel, R., 2014. New geological and geochronological data of the Placer de Guadalupe uplift, Mexico: a new piece of the Late Triassic early Jurassic Nazas Arc? Int. Geol. Rev. 56, 2000–2014.
White, W.B., 2008. Cave sediment and paleoclimate. J. Cave Karst Stud. 69 (1), 76–93.
Williams, W.J.W., 2002. Quaternary maar volcanism in the southern Rio Grande rift, New Mexico. Geological Society of America, 36th Annual Meeting, South-Central Section (Abstracts: http://gsa.confex.com/gsa/2002SC/finalprogram/abstract_32966.htm).
Wilson, D., Aster, R., West, M., Ni, J., Grand, S., Gao, Baldridge, W.S., Semken, S., Patel, P., 2005. Lithospheric structure of the Rio Grande rift. Nature 433, 851–855.
Wilson, I.F., Rochas, V.S., 1948. Manganese deposits of the Talamantes district near Parral, Chihuahua, Mexico. U.S. Geol. Surv. Bull. 954-E, 181–208.
Wilson, P.A., Jenkyns, H.C., Elderfield, H., Larson, L., 1997. The paradox of drowned carbonate platforms and the origin of Cretaceous Pacific guyots. Nature 392, 889–894.
Yoon, S.H., Sohn, Y.K., Chough, S.K., 2014. Tectonic, sedimentary, and volcanic evolution of a back-arc basin in the East Sea (Sea of Japan). Mar. Geol. 352, 70–88.